Author Manuscript

Author Manuscript

Author Manuscript

Author Manuscript

HHS Public Access

Author manuscript

Neuron. Author manuscript; available in PMC 2022 December 01.

Published in final edited form as:

Neuron. 2021 December 01; 109(23): 3838–3850.e8. doi:10.1016/j.neuron.2021.09.033.

Recruitment and inhibitory action of hippocampal axo-axonic cells during behavior

Barna Dudok[1,10,*,#], **Miklos Szoboszlay**[2,10], **Anirban Paul**[3,4,10], **Peter M. Klein**[1,10], **Zhenrui Liao**[2,10], **Ernie Hwaun**[1], **Gergely G. Szabo**[1], **Tristan Geiller**[2], **Bert Vancura**[2], **Bor-Shuen Wang**[4], **Sam McKenzie**[5,6], **Jesslyn Homidan**[1], **Lianne M. F. Klaver**[7], **Daniel F. English**[6,7], **Z. Josh Huang**[4,8,11], **György Buzsáki**[6,11], **Attila Losonczy**[2,9,11], **Ivan Soltesz**[1,11]

[1)]Department of Neurosurgery, Stanford University, Stanford, CA, 94305, USA

[2)]Department of Neuroscience, Columbia University, New York, NY, 10027, USA

[3)]Department of Neural and Behavioral Sciences, Penn State College of Medicine, Hershey, PA, 17033, USA

[4)]Cold Spring Harbor Laboratory, Cold Spring Harbor, New York, NY, 11724, USA

[5)]Department of Neurosciences, University of New Mexico, Albuquerque, NM, 87131, US

[6)]NYU Neuroscience Institute, New York University, New York, NY, 10016, USA

[7)]School of Neuroscience, Virginia Tech, Blacksburg, VA, 24061, USA

[8)]Department of Neurobiology, Duke University School of Medicine, Durham, NC, 27710, USA

[9)]Mortimer B. Zuckerman Mind Brain Behavior Institute, Columbia University, New York, NY, 10027, USA.

[10)]These authors contributed equally.

[11)]Senior author.

Summary

The axon initial segment of hippocampal pyramidal cells is a key subcellular compartment for action potential generation, under GABAergic control by the ‘chandelier’ or axo-axonic cells (AACs). Although AACs are the only cellular source of GABA targeting the initial segment, their *in vivo* activity patterns and influence over pyramidal cell dynamics are not well understood. We achieved cell type-specific genetic access to AACs in mice and show that AACs in the

[*]Correspondence: bdudok@stanford.edu.

Author contributions

Conceptualization, Z.J.H., G.B., A.L., and I.S.; Methodology, A.P., B.W and Z.J.H.; Formal analysis: B.D., Z.L. and E.H., Investigation, B.D., M.S., P.M.K., E.H., G.G.S., T.G., B.V., and J.H.; Writing – Original Draft, B.D., I.S., A.L., and G.B.; Writing – Review & Editing, all authors; Funding Acquisition, Z.J.H., G.B., A.L. and I.S.; Supervision, Z.J.H., G.B., A.L. and I.S.

[#]Lead contact

Declaration of interests

The authors declare no competing interests.

Publisher's Disclaimer: This is a PDF file of an unedited manuscript that has been accepted for publication. As a service to our customers we are providing this early version of the manuscript. The manuscript will undergo copyediting, typesetting, and review of the resulting proof before it is published in its final form. Please note that during the production process errors may be discovered which could affect the content, and all legal disclaimers that apply to the journal pertain.

Author Manuscript Author Manuscript Author Manuscript Author Manuscript

hippocampal area CA1 are synchronously activated by episodes of locomotion or whisking during rest. Bidirectional intervention experiments in head-restrained mice performing a random foraging task revealed that AACs inhibit CA1 pyramidal cells, indicating that the effect of GABA on the initial segments in the hippocampus is inhibitory *in vivo*. Finally, optogenetic inhibition of AACs at specific track locations induced remapping of pyramidal cell place fields. These results demonstrate brain state-specific dynamics of a critical inhibitory controller of cortical circuits.

Graphical Abstract

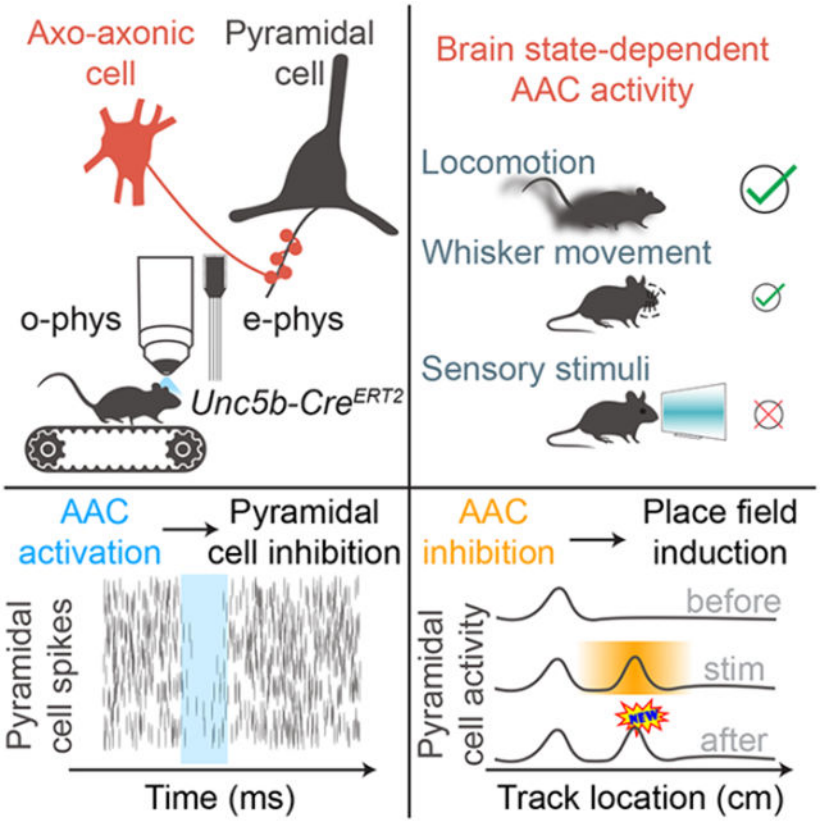

eTOC blurb

Dudok et al. introduce a transgenic mouse line for selectively labeling hippocampal axo-axonic cells (AACs). AACs are activated by movements in awake, behaving mice, and exert inhibitory postsynaptic effects on CA1 pyramidal cells. During a spatial navigation task, location-specific AAC silencing induces novel place fields in pyramidal cells.

Introduction

The site of action potential initiation in cortical pyramidal cells (PCs) is the axon initial segment (AIS) (Palay et al., 1968; Stuart et al., 1997). This highly specialized subcellular compartment exhibits the highest density of voltage-gated Na^+ channels anywhere on the neuronal surface, complemented by a unique molecular assembly of ion channels and cytoskeletal proteins (Howard et al., 2005; Huang and Rasband, 2018). The AIS of all

Author Manuscript Author Manuscript Author Manuscript Author Manuscript

neocortical and hippocampal PCs is under strong GABAergic control by a specialized interneuron type, the ‘chandelier’ or axo-axonic cell (AAC) (Somogyi, 1977). The AACs form synapses exclusively on the AIS of PCs, but not on interneurons, and thus they are strategically positioned to regulate action potential output of PCs and synchronize PC assemblies (Cobb et al., 1995; Li et al., 1992). Through their subcellular target specificity, AACs are the only cellular source that delivers GABA directly at the AIS, a feature that is also conserved in the human cortex (Fonseca et al., 1993; Del Río and DeFelipe, 1994).

Previous studies have provided anatomical, molecular, and *in vitro* physiological characterization of AACs (Buhl et al., 1994a, 1994b; Ganter et al., 2004). However, despite the presumed key role of AACs in controlling action potential initiation and timing, the *in vivo* characteristics of AAC activity dynamics and their effects on PC spiking in the hippocampus in behaving animals have remained incompletely understood. For example, although *in vivo* electrophysiological recordings have been obtained from post-hoc identified individual AACs in the hippocampus using the juxtacellular recording technique (Klausberger et al., 2003; Viney et al., 2013), even the largest such data set contains only seven cells in different animals (Varga et al., 2014). Similarly, recent *in vivo*, cellular-resolution, calcium imaging of pan-interneuronal activity in the CA1 combined with post-hoc identification in principle allows for the simultaneous assessment of several putative AACs per mouse (Geiller et al., 2020). However, a caveat of the latter approach for the specific case of AACs remains, as identification was based on the joint immunopositivity and immunonegativity of two neurochemical markers (parvalbumin (PV) and SATB1, respectively; see also below). Furthermore, these approaches do not allow the selective positive and negative manipulation of the activities of populations of AACs *in vivo*. Therefore, while these previous studies indicated a strong modulation of AAC spiking by theta oscillations associated with running and little AAC activity during ripple oscillations associated with quiet wakefulness, a major knowledge gap has remained regarding the recruitment and function of hippocampal AACs *in vivo*. On the basis of *in vitro* studies, it has been suggested that chloride-conducting $GABA_A$ receptors on the AIS may depolarize PCs (Perumal et al., 2021; Szabadics et al., 2006; Woodruff et al., 2009), but others reported a hyperpolarizing effect (Dugladze et al., 2012; Glickfeld et al., 2009; Woodruff et al., 2011). Since neurons *in vitro* can exhibit altered intracellular chloride homeostasis (Dzhala et al., 2012; Glykys and Staley, 2016; Glykys et al., 2017), the impact of GABA at AIS on PC spiking has remained to be determined by *in vivo* investigation.

To shed light on the *in vivo* recruitment and downstream effects of AACs, we developed a novel mouse line to gain genetic access to AACs. Large scale optical and electrical recordings in the CA1 region of the hippocampus in behaving mice revealed a coordinated increase in CA1 AAC activity at the onset of both locomotion and whisking episodes, but not in sharp wave-ripples (SPW-R) during immobility. Bidirectional perturbation experiments revealed that AACs efficiently inhibit PCs. Finally, we show that AAC inhibition at specific locations in mice performing a random foraging task induces CA1 place field remapping. Taken together, these results demonstrate the *in vivo* dynamics and functional impact of AACs in the control of PC spike initiation in the hippocampus.

Author Manuscript Author Manuscript Author Manuscript Author Manuscript

Results

The Unc5b-CreER line selectively labels hippocampal AACs

In order to enable critical genetic access to AACs in the hippocampus for *in vivo* recordings and interventions, we took advantage of the fact that *Unc5b*, a netrin receptor widely expressed in the developing nervous system, is largely restricted to AACs among cortical neurons in the postnatal brain (Paul et al., 2017) (note that AAC-enriched *Unc5b* expression is conserved even in humans (Bakken et al., 2020)). We generated a gene knockin mouse driver line *Unc5b-2A-Cre^{ERT2}* (referred to as Unc5b-CreER below) by inserting an in-frame T2A-Cre^{ERT2} cassette just before the STOP codon of the *Unc5b* gene (Fig 1A, see Methods). To characterize the expression pattern in Unc5b-CreER, we virally transduced a Cre-dependent fluorescent reporter (mCherry) in the CA1 region of adult mice of both sexes, followed by tamoxifen induction of recombination. Neurons were labeled predominantly in the strata (str.) pyramidale and oriens (see laminar distribution of cell bodies in Fig. 1B-C). As expected from AACs, the axonal arborization of the labeled cells was confined to the pyramidale and to the portion of the oriens closest to the pyramidale (Fig. 1A), with no axons visible in any of the dendritic layers of the CA1. Similarly to juxtacellularly labeled AACs (Klausberger et al., 2003; Varga et al., 2014; Viney et al., 2013), the dendrites of the Unc5b neurons extended all the way into the str. lacunosum-moleculare (Fig. S1A). The organization of axons into cartridge-like formations (Fig. 1D, S1B) further suggested the labeling of AACs (Buhl et al., 1994a). To corroborate this, we carried out three sets of experiments, using immunostaining, electron microscopy, and electrophysiology.

First, we performed immunostaining against IkBα, a protein regulator of transcription factors, the phosphorylated form of which (p-IkBα) is specifically enriched in AISs (Dugladze et al., 2012; Schultz et al., 2006). mCherry-positive axons studded with boutons preferentially made contacts with p-IkBα- labeled AISs (Fig. 1D). Analysis of confocal z-stacks of Unc5b-AAC axons in the str. pyramidale revealed that mCherry-positive voxels were near p-IkBα-positive objects (0.74 ± 0.26 μm, Fig. 1E, S1C-F), suggesting that the axons specifically target AISs. AACs are known to specifically innervate PCs but not interneurons (Somogyi, 1977), and indeed we observed Unc5b-AAC axons avoiding AISs of putative interneurons (Fig. S1B). To estimate the completeness of our AAC labeling, we identified PC AISs based on their innervation by PV-immunopositive axon terminals (Varga et al., 2014). Unc5b reporter-positive boutons were detected in 87 ± 10% of such AISs (Fig. S1D), indicating that most PC AISs are innervated by Unc5b-AACs. The expression pattern was similar between dorsal and ventral CA1 (Fig. S1E), and we focused on the former in the rest of the study. It should be also noted that, consistent with the large variability of neocortical AAC PV expression (Taniguchi et al., 2013), we observed a wide range of PV immunofluorescence in Unc5b-AAC somata, including some that appeared to be PV negative (Fig. S1B, see also Fig. S3C,D).

We next performed preembedding immunostaining and electron microscopy to independently assess the specificity of Unc5b-AAC axons to form synapses on AISs. Analysis of 54 immunopositive axonal profiles in the pyramidal and proximal oriens layers through serial sections revealed that the majority (88 ± 11%) of 27 synapse-forming axon

Author Manuscript Author Manuscript Author Manuscript Author Manuscript

terminals from 3 mice formed symmetric synapses on postsynaptic targets consistent with AISs (Fig. 1F-H). 25% of these were definitively identified as AISs based on ultrastructural markers (Buhl et al., 1994b; Palay et al., 1968), while the remaining profiles were classified as putative AIS (i.e., these structures were likely AISs, but the possibility that some were dendrites could not be entirely excluded). The low proportion of somatic synapses despite the dense axonal arborization near str. pyramidale (10 ± 11%) is in line with the reported specificity of AAC axons (Gour et al., 2021; Schneider-Mizell et al., 2020), and argues against the potential labeling of basket cells in Unc5b-CreER.

Finally, we characterized electrophysiological properties of Unc5b-AACs by performing fluorescence-targeted whole-cell patch-clamp recordings of somata near the pyramidal layer in acute hippocampal slices. Recorded cells (n = 50) were filled with biocytin and *post hoc* confirmation of axonal distribution was carried out on a subset of cells (Fig. 1l). Consistent with a specific labeling of CA1 AACs, all cells with visualized axons had axon arbors located at the str. pyramidale and oriens border, and axons successfully recovered after ρ-IkBα immunostaining contacted immunolabeled AISs (n = 11, Fig. 1J). Notably, none of the filled cells displayed basket cell-like axonal morphology (i.e., axons encircling somata in the str. pyramidale). The cell-intrinsic properties, including firing pattern and action potential waveform of Unc5b-AACs (Fig. 1L-M) were consistent with expected AAC firing patterns, including the relatively fast, sub-millisecond mean spike width and large after-hyperpolarization on average (Buhl et al., 1994b; Papp et al., 2013; Taniguchi et al., 2013). Principal component analysis on electrophysiological properties indicated no difference between the morphologically confirmed AACs and the other filled cells (Fig. S1H,I). However, there was a considerable degree of variability in Unc5b-AAC intrinsic properties (Fig. 1N), in agreement with previous reports (Buhl et al., 1994b; Ganter et al., 2004). Taken together, these results indicate that in the CA1, the Unc5b-CreER line enables viral delivery of genetically encoded indicators and actuators selectively to AACs adult mice.

In vivo recruitment of AACs is brain-state dependent and synchronous

To characterize AAC activity dynamics *in vivo*, we virally expressed the genetically encoded calcium indicator GCaMP6f (Chen et al., 2013) in CA1 AACs in Unc5b-CreER mice, alongside the red-shifted indicator jRGECO1a (Dana et al., 2016) in all CA1 neurons (Fig. 2A). Using dual-channel two-photon calcium imaging, we recorded Unc5b-AAC activity in head-fixed mice voluntarily running and resting on a linear treadmill. The local field potential (LFP) was recorded using silicone probes chronically implanted in the contralateral CA1 str. pyramidale (Dudok et al., 2021; Geiller et al., 2020), and mouse behavior was monitored by near-infrared video (Fig. 2A). These experiments revealed that AAC calcium signals (ΔF/F) were maximal during episodes of locomotion (Fig. 2B), exceeding the activation of other CA1 neurons (Fig. 2C, S2B). Because running is associated with hippocampal theta oscillations, this result is in agreement with the robust theta-rhythmic firing of individual AACs observed with juxtacellular recordings in previous studies (Klausberger et al., 2003; Varga et al., 2014; Viney et al., 2013). Note that the high firing rates of AACs relative to PCs are likely underestimated by GCaMP6f imaging (Rupprecht et al., 2021).

Author Manuscript Author Manuscript Author Manuscript Author Manuscript

Outside of ambulatory episodes, transient increases in AAC activity were also observed while mice were immobile (arrows in Fig. 2B), and these transients occurred simultaneously across multiple AACs (Fig. 2D). Overlaying AAC calcium traces with whisker movements revealed AAC activation at the onsets of whisking events (Fig. 2D, S2B), with larger transients occurring during longer whisking episodes ($r = 0.32$, $p < 0.001$, $n = 60502$ events × cells). Similarly to running, whisking in rodents belongs to theta-associated exploratory behaviors, however, in the absence of head movements, whisking in the air is not accompanied by hippocampal theta (Berg et al., 2006; Vanderwolf, 1969; Whishaw and Vanderwolf, 1971). During the immobility-associated whisking episodes in our head-fixed experiments, we observed a transient increase in gamma- but not in theta-band power (Fig. 2E). While AACs and other neurons were activated together at whisking event onset, AACs displayed sustained activity, contributing to a significantly higher integrated response in AACs (Fig. 2F, S2B). Additional experiments showed that the above-described cell type-specific differences in behavioral state-dependent neuronal activities were invariant to the choice of calcium indicators (Fig. S2B). To investigate whether AAC recruitment is specific to movements, we recorded AAC responses to visual or tactile stimuli. Stimulus presentation alone was not followed by AAC activation, with the latter being observed only in trials that also evoked active whisker movements (Fig. S2D). Comparing male and female mice revealed no sex differences in AAC responses during running, whisking or sensory stimuli (Fig. S2B,D).

In the absence of whisking in the stationary mouse, quiet wakefulness is known to give rise to SPW-Rs, synchronous population events involved in the replay of neuronal sequences (Buzsáki, 2015). In contrast to the intense firing of other PV cells, previous juxtacellular studies showed that most AACs are silent during SPW-Rs (Geiller et al., 2020; Klausberger et al., 2003; Varga et al., 2014; Viney et al., 2013), with a subset of AACs displaying moderately elevated spiking during SPW-R episodes (Varga et al., 2014). To analyze Unc5b-AAC recruitment during SPW-Rs, we first confirmed that the recruitment of non-AAC CA1 neurons during SPW-Rs detected from the contralateral LFP was readily observed using calcium imaging (median response = 12.7 $\Delta F/F$ %, $p < 0.0001$, one-sided Wilcoxon signed rank test, $n = 11194$ units). Next, we analyzed AAC responses with subframe precision, taking into account the delay between SPW-R onsets and the scanning of each AAC (see Methods). While the SPW-R related activity of about half of the Unc5b-AACs was at chance level (i.e., they appeared silent), 46-56% of AACs (depending on the calcium indicator) showed a small (median response = 2.4 $\Delta F/F$ %), but statistically significant fluorescence increase in SPW-Rs (Fig. 2F, S2C), in overall agreement with the juxtacellular reports. For any AAC, activation was detected in a minority of SPW-R episodes (<20%, Fig. S2C). SPW-Rs and whisking events were mutually exclusive, as demonstrated by a suppressed average whisking response during SPW-Rs and vice versa (Fig. 2D-F).

Overlaying traces from several AACs recorded simultaneously revealed coordinated activations across the AAC population (Fig. 2D). Indeed, quantification of the pairwise correlations of AAC units revealed that these cells were positively correlated (Pearson's $r > 0$ in 98% of AAC-AAC pairs, median = 0.35), at least at the temporal resolution of our calcium imaging (15.6 Hz). A positive correlation between AAC unit activity during running and whisking episodes (Fig. 2G) indicates that the same Unc5b-AAC population is recruited

Author Manuscript Author Manuscript Author Manuscript Author Manuscript

in both events. Analysis of AAC-AAC correlations in rolling ± 1 s time windows revealed that CA1 AACs are coactive at the initiation of locomotory and whisking behavior (Fig. 2H), while SPW-R onset during immobility was associated with reduced correlation (Fig. 2H), as expected from the weak and heterogenous SPW-R specific AAC activation (Fig. 2F, S2C). We previously found that the PV interneuron population (mostly comprised of basket cells, PVBCs) positively scales with ensemble activity, such that low-medium-high PV interneuron activity tightly tracks low-medium-high CA1 PC activity on the time scale of seconds (Dudok et al., 2021). In contrast, AAC population activity only weakly scaled with ensemble activity (i.e., average AAC activity was similar between low-medium-high CA1 ensemble activity) (Fig. 2I), except for at the very top of the range. Further analysis indicated that these epochs with high activity of AACs and other neurons correspond to locomotion (Fig. S2E).

Altogether, these results indicate that CA1 AAC activity is strongly modulated by brain state transitions *in vivo*. The AACs are coactive at the onset of both locomotion and whisking episodes but are not activated by sensory stimuli in the absence of movements. Furthermore, AACs are not reliably recruited by SPW-R events and their activity does not faithfully track fluctuations of PC ensemble activity, in contrast to other PV interneuron types.

AACs exert inhibitory postsynaptic effects on CA1 PCs in vivo

To directly determine the excitatory versus inhibitory effect of AAC inputs on the AIS, we assessed the effect of optogenetically driving AACs on PC activity using two complementary methods. First, we used acute silicone probes to record CA1 unit activity in head-fixed mice during spontaneously running and resting on a linear treadmill (Fig. 3A). The general cell types (interneuron or PC) of isolated units were classified based on spike waveform characteristics (Stark et al., 2013). AACs virally expressing channelrhodopsin (hChR2) under the control of Unc5b-CreER were optogenetically driven using blue laser light delivered through an optical fiber. In response to brief (20 ms) light pulses, we observed rapid reductions of PC firing rates (Fig. 3B). In contrast, a subset of putative interneurons responded to photostimuli with rapid activation (Fig. 3C, S3A). The action potential waveforms and spiking patterns of these opto-tagged cells were consistent with the properties of identified AACs recorded with the juxtacellular method, and none of the units had properties consistent with PVBCs (Klausberger et al., 2003; Varga et al., 2014; Viney et al., 2013) (Fig. S3A). The silicone probe recordings in the pyramidal layer also revealed photostimulation-evoked extracellular field potentials that were consistent with the extracellular field inhibitory postsynaptic potentials previously recorded *in vitro* and *in vivo* (Beyeler et al., 2013; Dubanet et al., 2020; Glickfeld et al., 2009) (Fig. 3D). Peak AAC activation was reliably followed by a prominent suppression of PC spiking (Fig. 3E-F), similar to an inhibition of PC action potential firing after optogenetic activation of AACs. Activation of PC units was rare and below the expected false positive rate (Fig. 3E). There was also a reduction in the firing rate of non-tagged interneurons after AAC activation (Fig. 3C), most likely due to network effects resulting from the reduction in PC firing.

In a complementary set of experiments, we expressed the red-shifted excitatory opsin ChRmine (Marshel et al., 2019) fused to the red static fluorophore mScarlet in Unc5b-

Author Manuscript Author Manuscript Author Manuscript Author Manuscript

AACs, together with GCaMP6f targeted to the entire CA1 neuronal population to allow the recording of neuronal activity using two-photon calcium imaging with simultaneous photostimulation (Fig. 3G-I) (Kaufman et al., 2020). Red light photostimulation caused a robust activation of AACs, as determined from GCaMP6f transients in mScarlet-expressing neurons during 2 s-long stimuli (Fig. 3J, S3E). The same stimuli reduced the number of transients in non-AAC neurons, the majority of which were PCs, in awake mice spontaneously running and resting on a linear treadmill (Fig. 3J-K). The number of AACs present in the stimulation light cone was estimated by performing a cell count on a z-stack containing the imaging field of view for each mouse; a volume of 0.049 ± 0.005 mm^3 including the pyramidal layer contained 45 ± 15 AACs per normalized field (914 ± 277 AACs / mm^3). To confirm that ChRmine was not expressed in PVBCs, which could also exert an inhibitory effect on PCs if driven optogenetically, we have performed immunostaining against SATB1, a transcription factor expressed in the nuclei of PVBCs but not AACs (Varga et al., 2014; Viney et al., 2013; Geiller et al., 2020). None of the ChRmine-expressing labeled cells were positive for SATB1 (Fig. S3C,D). Suppressing AAC activity with the inhibitory opsin eNpHR (Gradinaru et al., 2008) conversely significantly increased calcium transient rates in non-AAC neurons (Fig. 3J-K). The above-described bidirectional modulation of CA1 neuronal activity by AAC-targeted optogenetic manipulations indicates that AACs exert inhibitory control over CA1 PC firing *in vivo*, with no indication of a substantial PC subset being driven by AACs.

AAC-mediated regulation of hippocampal place fields

Our results showed that AACs exert an inhibitory control on their target CA1 PCs. We next asked whether such control plays a role in adjusting a well-known, behaviorally relevant function of pyramidal cells, as determined by the formation and maintenance of PC place fields (O'Keefe and Nadel, 1978). At the start of each recording session, head-fixed mice explored a cue-rich treadmill belt (5-10 laps, PRE, Fig. 4A, see also Fig. S4H), while neural activity was recorded using large-scale two-photon GCaMP6f imaging. During running in the PRE phase, PC place fields were readily observable (Fig. 4B) (Danielson et al., 2016). After the PRE phase with no stimulation, spatially locked photostimulation was delivered at a selected location of the treadmill, for 5 subsequent laps (STIM). The applied photostimulation method was previously shown to reach a sufficiently large part of the CA1 network to alter the place field map (Kaufman et al., 2020). In the last phase, mice ran additional laps until the end of the trial (POST, Fig. 4A). Changes in PC place fields were quantified by computing the population vector correlations. Interestingly, both AAC activation and inhibition was accompanied by reduced place field correlations between the PRE and POST phases, compared to unstimulated controls (ChRmine stim vs Ctrl: p=0.026, unpaired t-test; eNpHR stim vs Ctrl: p=0.04, unpaired t-test; n=6 mice in ChRmine, 9 in Ctrl, 5 in eNpHR) (Fig. 4C). Thus, AAC photostimulation appears sufficient to induce place field remapping. However, AAC activation or inhibition had opposite effects on PC place fields. Consistent with the inhibitory effect of AACs on PC firing rates (Fig. 3), we observed a transient disappearance of place fields near the STIM location during AAC photoexcitation (Fig. 4E, Fig. S4A,C). This is likely due to an AAC activation-mediated suppression of in-field calcium events in PCs that by chance were coding for the future STIM location in the PRE phase (Fig. 4E). Conversely, AAC inhibition induced novel place fields at the STIM

Author Manuscript Author Manuscript Author Manuscript Author Manuscript

location (Fig. 4E,F, S4D,F,G), likely due to increasing PC activity during the light pulses (Fig. 4E). AAC inhibition-induced PC activity was followed by a significant net gain of novel place fields at the STIM location (paired t-test, p=0.012; Fig. 4E,F, Fig. S4D). These new place fields formed immediately after stimulation and persisted until the end of the session (up to 20 laps) (Fig. S4G *top*). Consistently with previous reports (Deshmukh and Knierim, 2013; Geiller et al., 2017), place fields were enriched near belt cues (Fig. S4C, G *bottom*). However, since an uncued location was always chosen for the photostimulus zone, the presence of tactile cues on the belt does not explain the gain of place fields after AAC inhibition. Thus, our experiments support a role of AACs in regulating hippocampal place fields.

Discussion

We characterized the *in vivo* activity dynamics and postsynaptic action of hippocampal AACs using a novel Uncb5-CreER mouse line. Our results demonstrate that AAC activation is brain state-dependent and correlated with the onset of ambulatory and whisking episodes. The postsynaptic effect of AACs on PC spike generation is inhibitory and can remap place fields in the CA1 network.

AACs were first described by Szentagothai and Arbib (1974), who named these chandelier cells after the vertically oriented rows of presumed presynaptic axon terminals observable through a light microscope in Golgi stained material. They thought that such cartridges correspond to synapses on apical dendrites, but subsequent study by Somogyi (1977) clarified using electron microscopy that the chandelier cells selectively and exclusively form synapses on PC AISs. The functional relevance of the GABAergic innervation of the AIS has remained both enigmatic and controversial (Gallo et al., 2020; Howard et al., 2005; Inan and Anderson, 2014). Do AACs in cortical networks increase or decrease the excitability of postsynaptic PCs (Glickfeld et al., 2009; Lu et al., 2017; Pan-vazquez et al., 2020; Szabadics et al., 2006; Woodruff et al., 2009)? How do brain states or sensory inputs modulate AAC populations (Massi et al., 2012; Zhu et al., 2004)? Do AACs get activated in a fractionated or synchronous manner (Lu et al., 2017; Taniguchi et al., 2013)? Do AACs play a role in SPW-R events (Somogyi et al., 2014)? And does the activity of AACs scale with the activity of the CA1 neuronal ensemble, similar to PV-expressing interneurons in general (Dudok et al., 2021)? To date, the lack of experimental access to enable the selective labeling, monitoring, and manipulation of AACs *in vivo* has severely limited our ability to directly address these important questions.

Most Uncb5-AACs we observed in the CA1 region were fast spiking (exhibiting sub-millisecond spike width and large after-hyperpolarization) cells that formed symmetrical synapses predominantly on PC AISs (Fig. 1). Despite the dense axonal arborization in and near the PC layer, the labeled cells rarely synapsed on somata, indicating that the Unc5b-CreER line did not label the developmentally related, but functionally distinct PVBCs. While previously developed strategies allow AAC labeling by Tamoxifen induction during embryonic or early postnatal development (Ishino et al., 2017; Taniguchi et al., 2013), Unc5b-CreER advantageously allows induction in the adult. Taken together, these

Author Manuscript Author Manuscript Author Manuscript Author Manuscript

characteristics make the line ideally suited for viral delivery of activity indicators and actuators selectively to hippocampal AACs.

Previous reports have shown considerable heterogeneity in AAC anatomy, connectivity and physiology (Ganter et al., 2004; Lu et al., 2017; Varga et al., 2014; Wang et al., 2019). Indeed, we observed Unc5b-AAC heterogeneity in the laminar location of somata, PV content, and *in vitro* and *in vivo* electrophysiological properties such as spike waveform and activation by SPW-Rs (Figs. 1-3). However, we observed the coactivation of the Unc5b-AAC population during brain state transitions at the initiation of movement associated with running- and whisking behaviors (Fig. 2). A single AAC cartridge contains ~6 GABAergic terminals, and 1 AAC contacts ~1,200 PCs. In turn, multiple AACs (~6) converge on a single AIS (Bezaire and Soltesz, 2013). Our results indicate that despite their phenotypic heterogeneity, AACs may provide concerted functional output controlling the PC AIS (Bezaire and Soltesz, 2013), which may be required to efficiently block the initiation and antidromic invasion of action potentials to the somatodendritic domain of PCs (Dugladze et al., 2012; Schneider-Mizell et al., 2020). Temporal coordination of AAC activation takes place in the absence of AAC-to-AAC synaptic contacts, whereas PVBC-to-PVBC inhibition is thought to be critically important in organizing PVBC oscillatory activities (Wang and Buzsáki, 1996). Future studies will be needed to establish the contribution of electric coupling of the AAC population through gap junctions (Taniguchi et al., 2013; Woodruff et al., 2011) and their regulation by inhibitory or excitatory afferents (see below) in the emergence of AAC-AAC synchronization in behaving animals.

Our results revealed the strongest AAC activity during locomotion and whisking episodes, most likely associated with heightened arousal (Fig. 2), in agreement with the observation that visual cortex AAC activity correlates with pupil diameter (Schneider-Mizell et al., 2020). Neocortical AACs were shown to be activated in up-states of the prefrontal cortex (Massi et al., 2012), but not by sensory stimulation in the somatosensory cortex (Zhu et al., 2004), in line with our results showing that hippocampal AACs are not activated by sensory stimuli *per se* without a motor response. Hippocampal AACs are paced by rhythmic septal cells (Joshi et al., 2017), as well as by entorhinal afferents (Kiss et al., 1998), with the latter possibility also supported by the extension of Unc5b-AAC dendrites in the str. lacunosum-moleculare (Fig. S1). The coactivity of AACs and their PC targets in theta states indicates a role of AACs pacing PC activity, given the strong preference of AACs to fire after the peak of the theta oscillation, before other PV interneuron types fire and when PC activity is scarce (Klausberger et al., 2003; Varga et al., 2014). Interestingly, while AACs, PVBCs and PCs are all activated during heightened arousal and theta states, only PVBCs and PCs are prominently reactivated in SPW-Rs. Withdrawal of AIS inhibition by local or extrinsic inhibition of AACs has been proposed as a mechanism for disinhibiting PCs during SPW-Rs (Buzsáki, 1986; Somogyi et al., 2014; Varga et al., 2014; Viney et al., 2013).

Overall, our results provide novel insights into AAC function. First, optogenetically driving AACs inhibited the spiking and calcium signals of PCs both during baseline activity (Fig. 3) and in their place fields (Fig. 4). These findings demonstrate that axo-axonic input can efficiently veto action potential generation even when PCs are strongly excited. Second, spontaneous, physiological AAC activity controls PC firing and gates synaptic plasticity, as

Author Manuscript Author Manuscript Author Manuscript Author Manuscript

disinhibiting PCs by suppressing AACs leads to the induction of new place fields. Therefore, while spatial tuning of AACs appears to be low (Geiller et al., 2020) and it is not yet established under what conditions location-biased modulation of AACs may take place to contribute to remapping in behaving animals, these results indicate that AAC function is necessary for suppressing PC activity outside their place fields during exploration and AAC modulation is sufficient for reorganizing a spatial map of the environment.

STAR Methods

RESOURCE AVAILABILITY

Lead contact—Further information and requests for resources should be directed to and will be fulfilled by the Lead Contact, Barna Dudok (bdudok@stanford.edu).

Materials Availability—Further information and requests for mouse reagent should be directed to and will be fulfilled by Dr. Z. Josh Huang (josh.huang@duke.edu). Distribution of the Unc5b-CreER mouse line is restricted by MTA.

Data and Code Availability

- Source data for figures has been deposited at Mendeley Data. The DOI is listed in the key resources table. Raw microscopy and electrophysiology data reported in this paper will be shared by the lead contact upon request.
- Custom scripts used in this study has been deposited at Zenodo. The DOI is listed in the key resources table.
- Any additional information required to reanalyze the data reported in this paper is available from the lead contact upon request.

EXPERIMENTAL MODEL AND SUBJECT DETAILS

Animals—All procedures were carried out in accordance with NIH guidelines and with the approval of the Administrative Panel on Laboratory Animal Care of Stanford University, the Columbia University Institutional Animal Care and Use Committee or the Cold Spring Harbor Laboratory Institutional Animal Care and Use Committee. Unc5b-CreER mice were obtained from Z. Josh. Huang laboratory under a fully executed MTA, and maintained as homozygous, on a C57BL/6J background. Adult mice of both sexes (2 months and older) were used in all experiments. Mice were housed in groups of 2-5 animals on a normal diet and 12/12 light dark cycle.

Generation of Unc5b-2A-Cre^{ERT2} mouse—Gene targeting vectors were generated using PCR-based cloning approach as described before (He et al., 2016; Taniguchi et al., 2011). A T2A-Cre^{ERT2} cassette was inserted in frame immediately before the stop codon of the *Unc5b* gene. Targeting vectors were linearized and transfected into a 129SVj/B6 F1 hybrid ES cell line (V6.5, Open Biosystems). Positive ES cell clones were used to obtain male heterozygous mice following standard procedures as previously described (Taniguchi et al., 2011). The Frt-Neo-Frt cassette in the founder line was removed by breeding with Actin-Flpe transgenic mice (gift from Dr. Susan Dymecki, JAX Stock No: 005703).

Author Manuscript Author Manuscript Author Manuscript Author Manuscript

METHOD DETAILS

Viral injections—For anatomy, *in vitro* and *in vivo* electrophysiology, and calcium imaging with LFP experiments, mice were injected in the CA1 (dorsal CA1: 2.3mm posterior, 1.5 mm lateral, 1.45-1.35mm ventral to Bregma; ventral CA1: −3.5 mm posterior, 3.4 mm lateral, 3.5 mm ventral to Bregma) using a Hamilton syringe as previously described (Bui et al., 2018), with one or more of the following viruses: AAV1.Syn.Flex.GCaMP6f.WPRE.SV40, AAV5-EF1a-DIO-mCherry, AAV5-EF1a-DIO-hChR2-(H134R)-mCherry, AAV9-CAG-DIO-ChroME-ST-P2A-H2B-mRuby3, AAV1.Syn.NES-jRGECO1a.WPRE.SV40, AAVDJ-CaMKIIa-GCaMP6f, AAV1.Syn.Flex.NES-jRGECO1a.WPRE.SV40 (300-400 nl each, full titer), bilaterally (for anatomy and physiology) or in the right hemisphere (for calcium imaging).

For calcium imaging with optogenetics, mice were injected with AAV1.Syn.GCaMP6f.WPRE.SV40 in combination with either AAV1-Ef1a-DIO-ChRmine-mScarlet or AAV1-Ef1a-DIO-eNpHR3.0-EYFP with a Nanoject syringe, as previously described (Lovett-Barron et al., 2014). Briefly, mice were anesthetized with isoflurane and treated with analgesics (meloxicam). The skull was exposed, and a hole was drilled above the dorsal hippocampal CA1 (from Bregma AP −2.2 mm, ML −1.75 mm, and DV −1.2 mm, −1.1 mm, −1.0 mm, −0.9 mm with 64 nl of virus at each DV plane) through which a glass capillary was lowered into the brain.

Tamoxifen injections—Mice were anaesthetized with isoflurane and injected intraperitoneally (i.p.) with tamoxifen (100 mg/kg, Sigma) dissolved in corn oil (Sigma) at 20 mg/ml. For *in vivo* two-photon calcium imaging and optogenetics experiments, mice were injected with tamoxifen once running performance was sufficient (details of surgeries and training below). Expression was checked 2 days later, and if necessary, a second tamoxifen injection was administered. Recordings started 4 days after the first tamoxifen injection. For all other experiments, mice were injected with tamoxifen on days 2, 5 and 8 after virus injection.

Perfusions—Mice were anaesthetized by isoflurane, then injected i.p. with ketamine (100 mg/kg) and xylazine (10 mg/kg) in saline. The animals were transcardially perfused with saline (9 ml 0.9% NaCl for 1 minute) or with ice-cold Phosphate-Buffered Saline (PBS, 40 ml, for SATB1 immunostainings) and then with fixative solution (4% paraformaldehyde with or without 0.2% picric acid in 0.1 M phosphate buffer). The fixative also contained 0.5% glutaraldehyde for the mice used for electron microscopy (EM). The fixative volume was 200 ml for mice for EM, and 40-100 ml for all other mice. Perfused brains were then post-fixed in the same fixative solution for 2 h at RT on a shaker for EM samples, or 24 h at 4°C for other samples. Brains were sliced on a vibratome (VT 1200 S, Leica Biosystems). Immunostaining was carried out on free-floating coronal sections (60-75 μm). Sections from some animals were stored in 30% sucrose in PBS at −80 °C until immunostaining.

Fluorescent immunostaining—Sections were washed in 0.1 M phosphate buffer, blocked in 0.05 M tris-buffered saline (TBS) containing 0.03% Triton X-100 (Sigma-Aldrich) and 1% bovine serum albumin (Sigma-Aldrich). Sections were incubated overnight

Author Manuscript Author Manuscript Author Manuscript Author Manuscript

in one or more primary antibodies diluted in TBS: chicken anti-mCherry (1:1000, EnCor); chicken anti-GFP (1:3000, Aves); rabbit anti-phospho-IkBα (1:1000, CST), guinea pig anti-PV (1:1000, Swant). After washing with TBS, sections were incubated in secondary antibodies diluted in TBS (1 μg/ml, conjugated with CF405S, CF488A, CF568 or DyLight647, highly cross-absorbed, by Biotium or Thermo Fisher). Sections were then washed and mounted in Vectashield (Vector Laboratories).

Fluorescent double immunostaining for PV and SATB1 was performed as described previously (Geiller et al., 2020). Sections were permeabilized for 2x20 minutes in PBS with 0.3% Triton X-100. Blocking was then performed with 10% Normal Donkey Serum (Jackson ImmunoResearch, Catalog #017-000-121) in PBST (PBS with 0.3% Triton X-100) for 45 minutes. The sections were then incubated in a PBS solution containing primary antibodies (chicken anti-PV, 1:5000; and rabbit anti-SATB1, 1:1000) for one hour at room temperature, followed by 2 days at 4°C. After 2 days, the slices were washed 3x15 minutes in PBS and then incubated in a PBS solution containing a mixture of secondary antibodies (donkey anti-chicken DyLight 405, 1:300; and donkey anti-rabbit Alexa 647, 1:300, Jackson ImmunoResearch) for 2 hours at room temperature. The sections were then washed 5x15 minutes in PBS at room temperature. Finally, sections were mounted on glass slides in Fluoromount-G aqueous mounting medium (ThermoFisher Scientific) and coverslipped.

Confocal images were acquired on a Zeiss LSM 710 or LSM800 or a Nikon A1 confocal microscope using 10× 0.45 NA, 20× 0.8 NA or 63× 1.4 NA objectives.

Electron Microscopy—Electron microscopy was carried out on samples from mice expressing GCaMP6f under the control of *Unc5b*, after the mice underwent *in vivo* two-photon calcium imaging. Vibratome sections were washed in PBS followed by an ascending series of sucrose in PBS (10 to 30%). Sections were flattened on an aluminum plate and subjected to 3 cycles of freezing over liquid nitrogen and thawing over a hotplate. Sections were then washed in PBS, then TBS, and blocked in TBS containing 5% normal goat serum (Vector Laboratories). Then, sections were incubated in primary antibody (chicken anti-GFP, 1:3000) for 2 days on a shaker at 4 °C. After washing in TBS, sections were incubated in biotinylated secondary antibody (1:200, Vector Laboratories, 2 hrs. on RT), washed in TBS, and developed using Vectastain ABC and DAB substrate kits following the kit protocols (Vector), except that the DAB reagent concentration was reduced by half. After washing in PBS, sections were treated with Osmium tetroxide (1% w/v in PBS, 15 mins on ice), washed in PBS, dehydrated in an ascending series of ethanol (30-100%), and treated with Uranyl acetate (10% of saturated solution, 20 mins on ice) during the 70% ethanol step. Finally, sections were washed in acetonitrile prior to embedding in a mixture of acetonitrile and EMbed 812 (EMS, 1:1 for 1h, followed by 2:1 overnight). After embedding, sections were plated on glass slides, covered with glass coverslips treated with mold release agent, and baked (24 hrs., 65 °C).

From the embedded sections, blocks containing the CA1 pyramidale and oriens layers were cut and attached to molds. A series of 50 nm ultrathin sections were cut on an Ultramicrotome (Leica), and collected on slot grids. The grids were contrasted with lead

Author Manuscript Author Manuscript Author Manuscript Author Manuscript

citrate, and images were taken on a transmission electron microscope (JEM-1400, JEOL) equipped with a OneView (Gatan) camera.

Immunopositive boutons (identified based on the presence of synaptic vesicles) were located by a random search in the area proximal to the oriens-pyramidale layers in the central section of the series. Once a bouton was found, it was followed through serial sections (in both directions) until the profile ended, formed a synapse, or the series ended. Images were captured of each serial section at 5000-12000× magnification. At synaptic contact, higher magnification (up to 20000×) images were taken to confirm the ultrastructural signatures of synapses, together with lower magnification overview images to visualize the postsynaptic target element. Somata were identified by the presence of the nucleus, dendrites were identified by the presence of spines receiving asymmetric synapses. AISs were identified by the presence of fasciculated microtubuli, undercoating, and a high density of boutons forming symmetric synapses on the profile. DAB-positive profiles were sparse, and most AIS-impinging boutons were immunonegative. This is likely due to the limited penetration of the immunostaining, as well as to the reduced DAB reagent concentration and short development times (< 3 mins) used to avoid background amplification.

Imaging window surgery—Surgeries were performed after three days of postoperative recovery following viral injections. Mice were then surgically implanted with a glass imaging window (diameter: 3.0 mm, 64-0720, Warner), attached to a stainless steel cylindrical steel cannula (diameter: 3.0 mm, height: 1.5 mm, Ziggy's Tubes and Wires or Tegra Medical) with Narland optical adhesive as described previously (Lovett-Barron et al., 2014). Briefly, mice were anesthetized with isoflurane and treated with analgesics (meloxicam, or bupivacaine and buprenorphine), the skull was exposed and removed with a biopsy punch (3.0 mm in diameter). Dura and cortical layers were removed while flushing the brain with ice-cold PBS or cortex buffer (Holtmaat et al., 2009), to minimize bleeding. The cannula was inserted, secured with Vetbond and UV-curable glue, and a stainless steel headpost was attached to the skull with dental cement. Mice recovered in their home cage and were monitored for three days post-operatively.

Chronic electrode implants—For correlated two-photon and LFP recording, chronic silicone probes were implanted after the mice recovered from imaging window implant. A craniotomy was made and mice were head-fixed on a spherical treadmill as described previously (Szabo et al., 2017; Varga et al., 2014). During quiet wakefulness in awake mice, a single-shank, 4-channel linear silicone probe (Q1x4-3mm-100-177-HQ4_21mm, NeuroNexus) or a bipolar wire electrode (tungsten, 0.002", 0.5 mm tip separation, A-M systems) was lowered in the dorsal CA1 mirroring the virus injection site. LFP was continuously monitored for SPW-R events. Once a site with maximal ripple amplitude was reached, the probe was stabilized using UV-curable glue, and the connector was attached to the headbar implant with dental cement.

In vitro electrophysiology—Mice were deeply anesthetized by Ketamine/Xylazine (100 mg/kg and 10 mg/kg in saline, respectively) and then transcardially perfused with an ice-cold protective recovery solution containing (in mM): 92 NMDG, 26 $NaHCO_3$, 25 glucose, 20 HEPES, 10 $MgSO_4$, 5 Na-ascorbate, 3 Na-pyruvate, 2.5 KCl, 2 thiourea, 1.25 NaH_2PO_4,

Author Manuscript Author Manuscript Author Manuscript Author Manuscript

0.5 $CaCl_2$, titrated to a pH of 7.3-7.4 with HCl (Ting et al., 2014). Coronal slices (300 μm) containing the hippocampus were cut in ice-cold protective recovery solution using a vibratome (VT 1200S, Leica Biosystems). Brain slices were then incubated in 35°C protective recovery solution for 12 minutes. Hippocampal slices were then maintained in room temperature aCSF consisting of (in mM): 126 NaCl, 26 $NaHCO_3$, 10 glucose, 2.5 KCl, 2 $MgCl_2$, 2 $CaCl_2$, 1.25 NaH_2PO_4. All solutions were equilibrated with 95% O_2/5% CO_2.

Intracellular recordings were performed in a submerged chamber perfused with oxygenated aCSF at 2.5 ml/min and maintained at 33°C by a chamber heater (BadController V, Luigs and Neumann). Hippocampal neurons were visualized using DIC illumination on an Olympus BX61WI microscope (Olympus Microscopy) with an sCMOS camera (Flash 4.0 LT+, Hamamatsu). Epifluorescence illumination from a mercury lamp was used to identify Unc5b-CreER neurons based on mCherry fluorescence. Recording pipettes were pulled from thin-walled borosilicate capillary glass (King Precision Glass) using a P97 puller (Sutter Instruments) and were filled with (in mM): 126 K-gluconate, 10 HEPES, 4 KCl, 4 ATP-Mg, 0.3 GTP-Na, 10 phosphocreatine (pH-adjusted to 7.3 with KOH, osmolarity 290 mOsm), as well as 0.2% biocytin. Pipettes had a 3-5 MΩ tip resistance and pipette capacitance was neutralized for all recordings.

Whole cell recordings were performed on mCherry-positive neurons in the CA1 dorsal hippocampus. Firing properties were assessed during current injection steps (−100 to 350 pA, 1s) in neurons where the holding current was adjusted to maintain a resting membrane potential close to −65 mV and were repeated twice per neuron. Data were acquired in pClamp software (Molecular Devices) using a Multiclamp 700B amplifier (Molecular Devices), low-pass filtered at 2 kHz, and digitized at 10 kHz (Digidata 1440A, Molecular Devices).

After recording, brain slices were transferred into a fixative solution containing 4% paraformaldehyde and 0.2% picric acid in 0.1 M phosphate buffer for 24 hrs at 4°C. Brain slices were then embedded in 2% agarose and 50 μm coronal sections were prepared on a vibratome for fluorescent immunostaining and confocal imaging as already described. In addition to mCherry and phospho-IkBα staining, biocytin was labeled with the addition of AF488-strepavidin (1:1000, Life Technologies) simultaneously with the other secondary antibodies.

In vivo electrophysiology with optogenetics—Following virus injection, silicone sealant (Kwik-Cast™) was used to fill the craniotomy and to mark injection sites for later experiments. To restrain head during recording, metal head bars were implanted on the skulls of mice using Super Glue and dental cement. In vivo extracellular recording experiments were carried out at least 3 weeks after the day of virus injection. On the recording day, a craniotomy was performed at the injection site on isoflurane anesthetized mice. Next, the mice were head-restrained on a treadmill and allowed to recover from anesthesia while either a 32-channel (Poly10mm, NeuroNexus) or a 128-channel silicon probe (Yang et al., 2020) with an attached optical fiber was gradually lowered into dorsal CA1. Data were acquired continuously at 30 kHz using the Open Ephys acquisition system together with a unipolar-input recording headstage based on either a RHD2132 or a

Author Manuscript Author Manuscript Author Manuscript Author Manuscript

RHD2164 digital electrophysiology interface chip (Intan Technologies). Blue laser pulses (430-490 nM, 4.5 mW power) with a duration of 20 ms were delivered at 2 Hz to measure light-evoked responses. Offline spike sorting was performed using MountainSort (Chung et al., 2017) and Kilosort2 (https://github.com/MouseLand/Kilosort), followed by visual inspection using the open source software Phy (https://github.com/cortex-lab/phy). Units with a maximum spike amplitude of less than 50 μV were excluded from further analysis.

In vivo two-photon calcium imaging and LFP recordings—Imaging with correlated locomotion, video and LFP recording was performed as previously described (Dudok et al., 2021). A two-photon, 8 kHz resonant scanner microscope (Neurolabware), and a 16x objective (0.8 NA WI, Nikon) was used. Acquisition was controlled by Scanbox (Neurolabware). Treadmill movements were tracked using a quadrature encoder. Video frames of the right eye and whiskers were captured (Allied Vision Mako) at the start and middle of each microscopy frame. A single channel of the implanted chronic silicone probe referenced against the immersion bath was amplified (NPI ELC-03XS), and digitized (National Instruments DAC). Bipolar electrodes were recorded using a differential amplifier (Model 1700, A-M Systems). Recording sessions lasted approx. 10 minutes, during which the mice were freely running and resting on a 2 m-long treadmill belt. Visual stimuli consisted of vertical movement of a horizontal line displayed on an LED matrix (9 by 16) placed in from of the animals at 10 cm distance from the eyes (22 degrees diameter). The line was displayed at constant brightness throughout the session and was moved (8.5 deg/s) for 3 seconds on stimulus trigger. Tactile stimuli consisted of a motor-mounted probe placed in the center of the left whisker field. Upon stimulus trigger, the rod rotated 360 degrees in 3 seconds, brushing through all whiskers in a column. Stimuli were triggered automatically by a random process with 1/200 probability in each frame (12.8 s/trigger), with a minimum delay of 100 frames 6.4 s) between stimuli.

In vivo two-photon calcium imaging and optogenetics—A two-photon, 8 kHz resonant scanner (Bruker) was used for imaging. Imaging experiments were conducted with a Nikon 16x water immersion objective (0.8 NA, 3.0 mm WD) with 1.5x digital optical zoom. Excitation wavelength was 920 nm for the imaging experiments (laser: Coherent Ultra II). Identification of putative axo-axonic cells were performed with either the same laser tuned to 1030 nm (for the AAV1-Ef1a-DIO-eNpHR3.0-EYFP experiments shown in Figs. 3,4) or a red laser at 1070 nm (Coherent Fidelity, for the AAV-Ef1a-DIO-ChRmine-mScarlet experiments shown in Figs. 3,4). For optogenetic experiments, stimulation was performed with an ultrafast LED at 620 nm (Prizmatix). For all experiments, mice were trained on a random foraging task as described previously (Danielson et al., 2016). Briefly, after recovery from surgery, mice were water restricted and trained on a clueless burlap belt to seek randomly delivered water rewards. Once their performance was sufficiently good, mice were imaged on a 2 m-long cue-rich belt.

QUANTIFICATION AND STATISTICAL ANALYSIS

Statistical analysis and modeling—Statistical analysis and modeling were performed using Python and R. Plots were generated using Python and edited for style using Adobe Illustrator. Appropriate statistical tests were selected based on study design and data was

Author Manuscript Author Manuscript Author Manuscript Author Manuscript

checked for meeting the assumptions of the test, by inspecting Q-Q or residual plots. Reported measures of central tendency and error are mean ± standard error, unless otherwise specified. Tests are 2-sided unless otherwise specified. Sample sizes don't reflect repeated measures.

Confocal image analysis—To measure the laminar distribution of labeled cell bodies, tiled z-stacks of confocal images covering the entire CA1 were captured using a 10× objective with identical settings (e.g. laser power and gain) across animals, and analyzed in FIJI/ImageJ (NIH). On maximum intensity projections, the location of each cell body was marked (including all visible cell bodies), at the borders of oriens-pyramidale and pyramidale-radiatum were drawn to compute the distance of each cell from the layer borders. For plotting, the negative of the distances from the pyramidale border are shown for oriens cells. A 50 μm wide band is drawn on the plots to illustrate the position and extent of the str. pyramidale. The mean fluorescence intensity in each cell was measured in freehand shapes drawn to include the cell body and was then normalized relative to the maximum cell body intensity observed across all animals.

To compute the 3-dimensional distance between AAC processes and AISs, z-stacks (2 from each hemisphere of each animal) were taken of 90 × 90 × 570 nm voxel size using a 63× oil immersion objective, with identical settings across animals. To facilitate the quantification of axon distribution, image fields were selected to include axons on the oriens-pyramidale border and exclude cell bodies of AACs. Images were analyzed using Python after applying the Despeckle and Subtract Background functions in ImageJ. For the mCherry (AAC) channel, positive voxels were detected using the OTSU threshold of the stack histogram (cv2 package). For the p-IkBα channel, positive pixels were identified slice by slice using the local (4 μm^2) Moran's I method (pysal package). Voxels in which significant clustering was detected ($p < 0.05$, $z > 0$), and the brightness exceeded the stack OTSU threshold, were included as positive. Finally, a binary fill operation was performed slice by slice in both channels, objects were detected, and filtered by size (> 1 μm^2) using the scipy.ndimage package. The binary volume images were converted to point clouds to compute a sparse matrix using kd-trees (scipy.spatial package) to determine the 3-dimensional distances of mCherry-positive voxels from the nearest p-IkBα-positive neighbor, for point pairs within a 3 μm distance threshold. Thus, distances greater than this threshold were undetermined. Importantly, the detection method of p-IkBα-positive objects was set sufficiently stringently to avoid the inclusion of noise or background.

Quantification of the ratio of Unc5b-AAC-innervated AISs was performed using ImageJ macros. Thin z-stacks of the AAC reporter and immunostainings against p-IkBα and PV (38 x 83 x 470 nm voxel size) were recorded. Images were pre-processed (Despeckle, Gaussian Blur sigma=1) and z-projected. AISs were labeled blinded to the other channels, by drawing freehand lines along each AIS. Then, for measurement, lines were converted into areas with 5 microns thickness, and fluorescence intensity, as well as the number of positive pixels after thresholding (Huang method), was measured in each area. Images were rotated 90 degrees and measurements were repeated to obtain a sample for normalization. After inspecting the histogram of the ratio of PV-positive voxels from all measured AISs in all animals, the threshold to include objects was set to 0.2. AISs with fewer PV pixels could

Author Manuscript Author Manuscript Author Manuscript Author Manuscript

belong to cell types that don't receive axo-axonic input (i.e., interneurons), or short truncated AIS segments without axo-axonic input. For any included object, the fluorescence intensity measured in the Unc5b reporter channel was normalized to the average intensity of all AIS objects in the same image measured after rotation. Thus, normalized values greater than 1 indicate above chance level presence of labeling, and these AISs were categorized positive.

Analysis of in vitro electrophysiology—Input resistance was calculated from the change in steady-state membrane potential resulting from hyperpolarizing current injections, while sag was measured as the difference between the steady-state and peak negative potential during a −100 pA hyperpolarizing current injection. Action potential threshold was the voltage where the dV/dt prior to a detected event first exceeded 3 times the standard deviation. Width was the time an action potential, resampled at 100 kHz, exceeded the half-height between threshold and peak voltages. Afterhyperpolarization (AHP) was measured as the difference between an action potential threshold and the most negative potential within 30 ms after the event. Recordings were excluded for neurons with a resting membrane potential that could not be maintained at < −55 mV or where the input resistance was > 500 MΩ. Data analysis was performed using Clampfit (Molecular Devices) and custom written Python scripts. The following features were evaluated in principal component analysis: Rheobase, Hyperpolarization sag, Input resistance, Action potential (AP) height, AP threshold, AP width, Mean upstroke velocity, Mean Downstroke Velocity, Adaptation score, Burstiness score, Afterhyperpolarization (AHP), Fast AHP, Medium AHP. Partial reconstruction of a representative neuron was done in Adobe Illustrator based on maximum intensity projections of a confocal z-stack by drawing lines along dendrites and placing markers on axonal varicosities.

Analysis of in vivo electrophysiology and optogenetics—Light-evoked field IPSPs were measured by calculating the event-triggered LFP waveforms from the channel that had maximal power in the ripple band (presumably closest to the pyramidal layer). Units were classified as putative pyramidal neurons (n=495) or putative interneurons (n=128) based on their waveform features following a previously published method (Stark et al., 2013). Briefly, a 2-D Gaussian mixture model was fit to the spike width and valley-to-peak time of each unit's spike waveform. Units close to the border of two clusters ($p>0.05$) were not classified (n=82). To identify optically responsive units, the parameter-free statistical test Zenith of Event-based Time-locked Anomalies (ZETA) was used (Montijn et al., 2020). This method first aligned spike time of each unit to an event of interest (i.e., onset of optical stimulation) and obtained a cumulative distribution of the aligned time. Significant deviation from the diagonal line on the cumulative graph ($p<0.01$) reflected modulation of spiking activity with respect to the event of interest. Moreover, peak or trough firing rate of a unit had to range from 1 ms to 50 ms to be considered significantly modulated. Units that were positively modulated were labeled as putative axo-axonic cells.

Image processing and analysis of calcium imaging with video and LFP—Calcium movies were pre-processed, cells were segmented, and ΔF/F traces were computed as described previously (Dudok et al., 2021). Motion correction was performed and regions of interest (ROIs) were detected using SIMA (Kaifosh et al., 2014). Unc5b-AAC ROIs

Author Manuscript Author Manuscript Author Manuscript Author Manuscript

were segmented using the *STICA* method of SIMA or manually drawn. Other neurons were segmented using the *PlaneCA1PC* method of SIMA. Multiple imaging sessions of the same field of view were matched, and individual AACs were assigned unique IDs and tracked across sessions. Unitary response properties were calculated for AACs based on all events detected in all sessions. ROIs of non-AAC units were not matched across sessions.

Event-triggered average responses: Whisking events were detected from video recordings. First, a motion energy map was computed for each frame (Powell et al., 2015), and the absolute sum across a cropped region containing the mouse was processed into baseline-corrected z-scored traces. Next, positive frames were identified as z-scored motion energy greater than 1. Frames were clustered using DBSCAN (eps = 1 s), and single frames and the first frames of clusters were included as event onset times. Lastly, an event-triggered average motion map was computed, and cropped to a subregion to only include whiskers as a source of movement. The motion energy trace and event detection were re-computed from this cropped region to obtain whisking event onsets. Events were not curated manually.

LFP power was determined by integrating the envelope of the band-pass filtered trace over the duration of each frame. Analysis of correlated activity. SPW-Rs were detected automatically from LFP traces, and curated manually, blind to calcium responses (Dudok et al., 2021; Varga et al., 2014). Clusters of events were included only once at the onset of the first event of the cluster, as described above. To determine the fraction of evets with significant AAC response, the differential of the traces was computed, and samples measured between 0-100 ms after SPW-R onset (ripple-band envelope crossing the threshold) were selected for each event. Delays between SPW-R detection (from traces downsampled to 1 kHz) and scanning the cell (~8000 lines per second) were determined with sub-frame precision, considering the position (row) of the cell within the frame. The maximum dF/dt value in the included samples was considered the SPW-R response. This was compared to a sample of random events analyzed the same way. Random events (n = 1000) were picked in frames without running (speed = 0), whisking (whisking < median) and ripple activity (ripple power < median). Random event onset times were picked with 0.1 ms precision. SPW-R responses exceeding 95% of random event responses were included as significant.

To compute event-triggered average calcium traces, masks around the event onsets were determined such that there was no overlap allowed between consecutive events (that is, imaging frames were only included in the ‘after’ average up until the next event, and the same logic was applied to ‘before’ frames. In case of closely spaced events, a conservative gap of 400 ms was enforced for including frames in the average for consecutive events, to account for the decay time constant of calcium indicators. For SPW-R and whisking events, traces were only included until the mouse stayed immobile. For running onset, frames were included regardless of locomotion. Events were first averaged by individual ROI ID (used for statistical analysis), then by cell type (used for plotting). The number used to calculate SEM was the number of cells in which at least one observation was recorded in the given time point. The process of event detection and averaging was fully automated to remove investigator bias. For plotting SPW-R responses with subframe precision, the DF/F traces

Author Manuscript Author Manuscript Author Manuscript Author Manuscript

of each event and cell were shifted by the measured delay, corrected for baseline (average between −1 to −0.1 s), and averaged in 20 ms time bins.

To determine cell type- and sex-specific differences in responses, linear mixed effects models were constructed (Response ~ CellType + Sex + (1|Animal)) and compared to null models omitting either cell type or sex using ANOVA. The effect of evoked whisking during sensory stimulation on AAC responses were determined for each stimulus type using a similar approach (Response ~ EvokedWhisking + Sex + (1|Animal)).

Unit-unit correlations were determined as Pearson's correlation coefficient between the full ΔF/F traces. Time-resolved correlation was computed in rolling windows (±1 s before and after each frame). Population-population correlations between AACs and 'Other' cells were computed as described previously (Dudok et al., 2021). Briefly, z-scored ΔF/F traces from all cells were averaged by cell type, resampled into non-overlapping time bins (bin size setting varied from 0.1 s to 10 s (in 0.1 s increments), normalized between 0 and 1. A temporal shift was applied to one of the traces (from −10 to 10 s, in 0.1 s increments) before the binning. The bins were then sorted based on the 'Other' values and the same sorting was applied to the 'AAC' values. The R_{AAC} x R_{Other} metric was computed for each bin size and offset setting. This metric measures correlated fluctuations between the two cell types, without returning spuriously high values in cases when fluctuations are averaged out (Dudok et al., 2021).

Image processing and analysis of calcium imaging with optogenetics—Imaging data were pre-processed using the SIMA, Suite2p and TreFiDe software packages (Buchanan et al., 2019; Kaifosh et al., 2014; Pachitariu et al., 2016). Motion correction was performed using whole frame registration. We used the Suite2p software package to segment spatial masks corresponding to neural ROIs, extract associated fluorescence signal within these spatial footprints, correcting for cross-ROI and neuropil contamination, and compute ΔF/F traces for each cell. Identified ROIs were curated post-hoc in the Suite2p graphical interface to exclude non-somatic components. ROI detection with Suite2p is inherently activity-dependent, so for each session, we detected only a subset of neurons present in the field of view.

Stimulation responsiveness and calcium event calculation: The *responsiveness* of a cell to a given stimulus under a given activity metric m (e.g., calcium transients) was defined as Σm_{stim} - Σm_{pre}, where m_{stim} is the value of the metric inside the stimulus window, and m_{pre} is the same metric in an identical-width window immediately preceding the onset of the stimulus. Calcium transients were conservatively identified as frames in which ΔF/F exceeded 150% of baseline. To determine the effect of photostimulus on the number of transients, linear mixed effects models were constructed (Transients ~ Stim + (1|Animal)) and compared to null models omitting Stim using ANOVA.

Identification of spatially tuned cells: Lap-by-lap tuning curves were calculated by dividing the 2m long, cued belt into 100 equal bins and computing the mean ΔF/F of each cell in each bin during running epochs for each lap. These lap-by-lap tuning curves were then smoothed with a Gaussian window with sigma=3 bins and averaged over laps for

Author Manuscript Author Manuscript Author Manuscript Author Manuscript

each cell to compute that cell's tuning curve. A null distribution for place fields was then computed by shuffling the underlying lap-by-lap tuning curves 100 times: bins where the cell's activity exceeded the 99th percentile of the shuffle distribution were identified as place fields. Place fields detected in this way were then filtered to those detected consistently in the same location on at least 3 laps.

Place field remapping: Population vector correlations were computed for every pair of spatial bins (Danielson et al., 2016) within the PRE, STIM, and POST laps. If no remapping occurs, the population vector correlation should resemble a perfect diagonal matrix in all of these conditions.

The degree of remapping of place fields in response to AAC manipulation was quantified via the average Pearson correlation the PRE stimulation population vectors with their counterparts in POST. Remapping is known to occur with the passage of time; therefore, this change was compared to unstimulated control sessions divided into PRE, STIM, and POST by lap number. Lower correlation values between population vectors indicate to a higher degree of remapping.

Place field turnover and novel place field formation: To investigate the contribution of in-zone place field turnover and novel place field formation to remapping, we examined place fields in the quintile of the belt centered around the stimulation zone. We constructed 2x2 contingency tables of cells with and without a place field in PRE sessions x with and without a place field in POST sessions for AAC excitation and inhibition. The diagonal entries represent cells with stable place fields (or lack thereof) in zone in both conditions. The off-diagonal entries represent place cell turnover: cells that either lost or gained place fields in the stimulation zone from PRE to POST. We interrogated the significance of this turnover using the McNemar-Bowker test (Bowker, 1948).

Supplementary Material

Refer to Web version on PubMed Central for supplementary material.

Acknowledgements

Research reported in this publication was supported by the National Institute of Neurological Disorders and Stroke (NINDS) and National Institute of Mental Health (NIMH) of the National Institutes of Health (NIH) under Award Numbers NINDSR01NS99457 (to IS), U19NS104590 (to IS, AL, and GB), K99NS117795 (to BD), NIMH1R01MH124047, NIMH1R01MH124867 NINDS1U01NS115530 (to AL), 5R01MH094705-04 (to ZJH), NINDS1F31NS120783 and NIGMST32GM007367 (to ZL), NIHT32GM007367 and NIMH1F30MH125628 (to BV), 5T32NS007280 (to PMK and EH), NIH5F32NS096877-03 (to BSW) and the Kavli Foundation (to AL). The content is solely the responsibility of the authors and does not necessarily represent the official views of the NIH. We thank the Stanford Neuroscience Gene Vector and Virus Core for providing AAV vector services, and Andrew Olson and the Stanford Neuroscience Microscopy Service, supported by NIH NS069375, for providing microscopy support; we are also grateful to John Perrino and Ruth Yamawaki and the Cell Science Imaging Facility Electron Microscopy Core at Stanford for help with electron microscopy. We thank Sylwia Felong, Anna Ortiz, and Sandra Linder for technical and administrative support.

Author Manuscript Author Manuscript Author Manuscript Author Manuscript

References

Bakken TE, Jorstad NL, Hu Q, Lake BB, Tian W, Kalmbach BE, Crow M, Hodge RD, Krienen FM, Sorensen SA, et al. (2020). Evolution of cellular diversity in primary motor cortex of human, marmoset monkey, and mouse. BioRxiv 10.1101/2020.03.31.016972.

Berg RW, Whitmer D, and Kleinfeld D (2006). Exploratory whisking by rat is not phase locked to the hippocampal theta rhythm. J. Neurosci 26, 6518–6522. [PubMed: 16775139]

Beyeler A, Retailleau A, Molter C, Mehidi A, Szabadics J, and Leinekugel X (2013). Recruitment of Perisomatic Inhibition during Spontaneous Hippocampal Activity In Vitro. PLoS One 8, e66509. [PubMed: 23805227]

Bezaire MJ, and Soltesz I (2013). Quantitative assessment of CA1 local circuits: knowledge base for interneuron-pyramidal cell connectivity. Hippocampus 23, 751–785. [PubMed: 23674373]

Bowker AH (1948). A Test for Symmetry in Contingency Tables. J. Am. Stat. Assoc 43, 572–574. [PubMed: 18123073]

Buchanan EK, Kinsella I, Zhou D, Zhu R, Zhou P, Gerhard F, Ferrante J, Ma Y, Kim S, Shaik M, et al. (2019). Penalized matrix decomposition for denoising, compression, and improved demixing of functional imaging data. BioRxiv 10.1101/334706.

Buhl EH, Halasy K, and Somogyi P (1994a). Diverse sources of hippocampal unitary inhibitory postsynaptic potentials and the number of synaptic release sites. Nature 368, 823–828. [PubMed: 8159242]

Buhl EH, Han ZS, Lorinczi Z, Stezhka VV, Karnup SV, and Somogyi P (1994b). Physiological properties of anatomically identified axo-axonic cells in the rat hippocampus. J. Neurophysiol 71, 1289–1307. [PubMed: 8035215]

Bui AD, Nguyen TM, Limouse C, Kim HK, Szabo GG, Felong S, Maroso M, and Soltesz I (2018). Dentate gyrus mossy cells control spontaneous convulsive seizures and spatial memory. Science 359, 787–790. [PubMed: 29449490]

Buzsáki G (1986). Hippocampal sharp waves: Their origin and significance. Brain Res. 398, 242–252. [PubMed: 3026567]

Buzsáki G (2015). Hippocampal sharp wave-ripple: A cognitive biomarker for episodic memory and planning. Hippocampus 25, 1073–1188. [PubMed: 26135716]

Chen T-W, Wardill TJ, Sun Y, Pulver SR, Renninger SL, Baohan A, Schreiter ER, Kerr RA, Orger MB, Jayaraman V, et al. (2013). Ultrasensitive fluorescent proteins for imaging neuronal activity. Nature 499, 295–300. [PubMed: 23868258]

Chung JE, Magland JF, Barnett AH, Tolosa VM, Tooker AC, Lee KY, Shah KG, Felix SH, Frank LM, and Greengard LF (2017). A Fully Automated Approach to Spike Sorting. Neuron 95, 1381–1394.e6. [PubMed: 28910621]

Cobb SR, Buhl EH, Halasy K, Paulsen O, and Somogyi P (1995). Synchronization of neuronal activity in hippocampus by individual GABAergic interneurons. Nature 378, 75–78. [PubMed: 7477292]

Dana H, Mohar B, Sun Y, Narayan S, Gordus A, Hasseman JP, Tsegaye G, Holt GT, Hu A, Walpita D, et al. (2016). Sensitive red protein calcium indicators for imaging neural activity. Elife 5, 1–24.

Danielson NB, Zaremba JD, Kaifosh P, Bowler J, Ladow M, and Losonczy A (2016). Sublayer-Specific Coding Dynamics during Spatial Navigation and Learning in Hippocampal Area CA1. Neuron 91, 652–665. [PubMed: 27397517]

Deshmukh SS, and Knierim JJ (2013). Influence of local objects on hippocampal representations: Landmark vectors and memory. Hippocampus 23, 253–267. [PubMed: 23447419]

Dubanet O, Ferreira Gomes Da Silva A, Frick A, Hirase H, Beyeler A, and Leinekugel X (2020). Probing the Polarity of Spontaneous Perisomatic GABAergic Synaptic Transmission in the Mouse CA3 Circuit in Vivo. SSRN Electron. J 36, 109381.

Dudok B, Klein PM, Hwaun E, Lee BR, Yao Z, Fong O, Bowler JC, Terada S, Sparks FT, Szabo GG, et al. (2021). Alternating sources of perisomatic inhibition during behavior. Neuron 109, 997–1012.e9. [PubMed: 33529646]

Dugladze T, Schmitz D, Whittington MA, Vida I, and Gloveli T (2012). Segregation of axonal and somatic activity during fast network oscillations. Science 336, 1458–1461. [PubMed: 22700932]

Author Manuscript Author Manuscript Author Manuscript Author Manuscript

Dzhala V, Valeeva G, Glykys J, Khazipov R, and Staley K (2012). Traumatic alterations in GABA signaling disrupt hippocampal network activity in the developing brain. J. Neurosci 32, 4017–4031. [PubMed: 22442068]

Fonseca M, Soriano E, Ferrer I, Martinez A, and Tuñon T (1993). Chandelier cell axons identified by parvalbumin-immunoreactivity in the normal human temporal cortex and in Alzheimer's disease. Neuroscience 55, 1107–1116. [PubMed: 8232900]

Gallo NB, Paul A, and Aelst L Van (2020). Shedding Light on Chandelier Cell Development, Connectivity , and Contribution to Neural Disorders. Trends Neurosci. 43, 565–580. [PubMed: 32564887]

Ganter P, Szücs P, Paulsen O, and Somogyi P (2004). Properties of horizontal axo-axonic cells in stratum oriens of the hippocampal CA1 area of rats in vitro. Hippocampus 14, 232–243. [PubMed: 15098728]

Geiller T, Royer S, and Choi J-S (2017). Segregated Cell Populations Enable Distinct Parallel Encoding within the Radial Axis of the CA1 Pyramidal Layer. Exp. Neurobiol 26, 1. [PubMed: 28243162]

Geiller T, Vancura B, Terada S, Troullinou E, Chavlis S, Tsagkatakis G, Tsakalides P, Ócsai K, Poirazi P, Rózsa BJ, et al. (2020). Large-Scale 3D Two-Photon Imaging of Molecularly Identified CA1 Interneuron Dynamics in Behaving Mice. Neuron 108, 968–983.e9. [PubMed: 33022227]

Glickfeld LL, Roberts JD, Somogyi P, and Scanziani M (2009). Interneurons hyperpolarize pyramidal cells along their entire somatodendritic axis. Nat. Neurosci 12, 21–23. [PubMed: 19029887]

Glykys J, and Staley KJ (2016). Developmental Decrease of Neuronal Chloride Concentration Is Independent of Trauma in Thalamocortical Brain Slices. PLoS One 11, e0158012. [PubMed: 27337272]

Glykys J, Dzhala V, Egawa K, Kahle KT, Delpire E, and Staley K (2017). Chloride Dysregulation, Seizures, and Cerebral Edema: A Relationship with Therapeutic Potential. Trends Neurosci. 40, 276–294. [PubMed: 28431741]

Gour A, Boergens KM, Heike N, Hua Y, Laserstein P, Song K, and Helmstaedter M (2021). Postnatal connectomic development of inhibition in mouse barrel cortex. Science 371, eabb4534. [PubMed: 33273061]

Gradinaru V, Thompson KR, and Deisseroth K (2008). eNpHR: a Natronomonas halorhodopsin enhanced for optogenetic applications. Brain Cell Biol. 36, 129–139. [PubMed: 18677566]

He M, Tucciarone J, Lee SH, Nigro MJ, Kim Y, Levine JM, Kelly SM, Krugikov I, Wu P, Chen Y, et al. (2016). Strategies and Tools for Combinatorial Targeting of GABAergic Neurons in Mouse Cerebral Cortex. Neuron 91, 1228–1243. [PubMed: 27618674]

Holtmaat A, Bonhoeffer T, Chow DK, Chuckowree J, De Paola V, Hofer SB, Hübener M, Keck T, Knott G, Lee W-CA, et al. (2009). Long-term, high-resolution imaging in the mouse neocortex through a chronic cranial window. Nat. Protoc 4, 1128–1144. [PubMed: 19617885]

Howard A, Tamas G, and Soltesz I (2005). Lighting the chandelier: New vistas for axo-axonic cells. Trends Neurosci. 28, 310–316. [PubMed: 15927687]

Huang CY-M, and Rasband MN (2018). Axon initial segments: structure, function, and disease. Ann. N. Y. Acad. Sci 1420, 46–61. [PubMed: 29749636]

Inan M, and Anderson SA (2014). The chandelier cell, form and function. Curr. Opin. Neurobiol 26, 142–148. [PubMed: 24556285]

Ishino Y, Yetman MJ, Sossi SM, Steinecke A, Hayano Y, and Taniguchi H (2017). Regional cellular environment shapes phenotypic variations of hippocampal and neocortical chandelier cells. J. Neurosci 37, 9901–9916. [PubMed: 28912162]

Joshi A, Salib M, Viney TJ, Dupret D, and Somogyi P (2017). Behavior-Dependent Activity and Synaptic Organization of Septo-hippocampal GABAergic Neurons Selectively Targeting the Hippocampal CA3 Area. Neuron 96, 1342–1357.e5. [PubMed: 29198757]

Kaifosh P, Zaremba JD, Danielson NB, and Losonczy A (2014). SIMA: Python software for analysis of dynamic fluorescence imaging data. Front. Neuroinform 8, 80. [PubMed: 25295002]

Kaufman AM, Geiller T, and Losonczy A (2020). A Role for the Locus Coeruleus in Hippocampal CA1 Place Cell Reorganization during Spatial Reward Learning. Neuron 105, 1018–1026.e4. [PubMed: 31980319]

Author Manuscript Author Manuscript Author Manuscript Author Manuscript

Kiss J, Buzsaki G, Morrow JS, Glantz SB, and Leranth C (1998). Entorhinal cortical innervation of parvalbumin-containing neurons (basket and chandelier cells) in the rat ammon's horn. Hippocampus 6, 239–246.

Klausberger T, Magill PJ, Márton LF, Roberts JDB, Cobden PM, Buzsáki G, and Somogyi P (2003). Brain-state- and cell-type-specific firing of hippocampal interneurons in vivo. Nature 421, 844–848. [PubMed: 12594513]

Li XG, Somogyi P, Tepper JM, and Buzsáki G (1992). Axonal and dendritic arborization of an intracellularly labeled chandelier cell in the CA1 region of rat hippocampus. Exp. Brain Res 90, 519–525. [PubMed: 1385200]

Lovett-Barron M, Kaifosh P, Kheirbek MA, Danielson N, Zaremba JD, Reardon TR, Turi GF, Hen R, Zemelman BV, and Losonczy A (2014). Dendritic inhibition in the hippocampus supports fear learning. Science 343, 857–863. [PubMed: 24558155]

Lu J, Tucciarone J, Padilla-Coreano N, He M, Gordon JA, and Huang ZJ (2017). Selective inhibitory control of pyramidal neuron ensembles and cortical subnetworks by chandelier cells. Nat. Neurosci 20, 1377–1383. [PubMed: 28825718]

Marshel JH, Kim YS, Machado TA, Quirin S, Benson B, Kadmon J, Raja C, Chibukhchyan A, Ramakrishnan C, Inoue M, et al. (2019). Cortical layer-specific critical dynamics triggering perception. Science 365, eaaw5202. [PubMed: 31320556]

Massi L, Lagler M, Hartwich K, Borhegyi Z, Somogyi P, and Klausberger T (2012). Temporal Dynamics of Parvalbumin-Expressing Axo-axonic and Basket Cells in the Rat Medial Prefrontal Cortex In Vivo. J. Neurosci 32, 16496–16502. [PubMed: 23152631]

Montijn JS, Seignette K, Howlett MH, Cazemier JL, Kamermans M, Levelt CN, and Heimel JA (2020). A parameter-free statistical test that improves the detection of neuronal responsiveness. BioRxiv 10.1101/2020.09.24.311118.

O'Keefe J, and Nadel L (1978). The Hippocampus as a Cognitive Map (Oxford: Clarendon Press).

Pachitariu M, Stringer C, Dipoppa M, Schröder S, Rossi LF, Dalgleish H, Carandini M, and Harris K (2016). Suite2p: beyond 10,000 neurons with standard two-photon microscopy. BioRxiv 10.1101/061507.

Palay SL, Sotelo C, Peters A, and Orkand PM (1968). THE AXON HILLOCK AND THE INITIAL SEGMENT. J. Cell Biol 38, 193–201. [PubMed: 5691973]

Pan-vazquez A, Wefelmeyer W, Sabater VG, Neves G, Burrone J, Pan-vazquez A, Wefelmeyer W, Sabater VG, and Neves G (2020). Activity-Dependent Plasticity of Axo-axonic Synapses at the Axon Initial Segment Article Activity-Dependent Plasticity of Axo-axonic Synapses at the Axon Initial Segment. Neuron 1–12.

Papp OI, Karlócai MR, Tóth IE, Freund TF, and Hájos N (2013). Different input and output properties characterize parvalbumin-positive basket and Axo-axonic cells in the hippocampal CA3 subfield. Hippocampus 23, 903–918. [PubMed: 23733415]

Paul A, Crow M, Raudales R, He M, Gillis J, and Huang ZJ (2017). Transcriptional Architecture of Synaptic Communication Delineates GABAergic Neuron Identity. Cell 171, 522–539.e20. [PubMed: 28942923]

Perumal MB, Latimer B, Xu L, Stratton P, Nair S, and Sah P (2021). Microcircuit mechanisms for the generation of sharp-wave ripples in the basolateral amygdala: A role for chandelier interneurons. Cell Rep. 35.

Powell K, Mathy A, Duguid I, and Häusser M (2015). Synaptic representation of locomotion in single cerebellar granule cells. Elife 4, 1–18.

Del Río MR, and DeFelipe J (1994). A study of SMI 32-stained pyramidal cells, parvalbumin-immunoreactive chandelier cells, and presumptive thalamocortical axons in the human temporal neocortex. J. Comp. Neurol 342, 389–408. [PubMed: 7517410]

Rupprecht P, Carta S, Hoffmann A, Echizen M, Blot A, Kwan AC, Dan Y, Hofer SB, Kitamura K, Helmchen F, et al. (2021). A database and deep learning toolbox for noise-optimized, generalized spike inference from calcium imaging. Nat. Neurosci 24, 1324–1337. [PubMed: 34341584]

Schneider-Mizell CM, Bodor AL, Collman F, Brittain D, Bleckert AA, Dorkenwald S, Turner NL, Macrina T, Lee K, Lu R, et al. (2020). Chandelier cell anatomy and function reveal a variably distributed but common signal. BioRxiv 10.1101/2020.03.31.018952.

Author Manuscript Author Manuscript Author Manuscript Author Manuscript

Schultz C, König H-G, Del Turco D, Politi C, Eckert GP, Ghebremedhin E, Prehn JHM, Kögel D, and Deller T (2006). Coincident enrichment of phosphorylated IkBα, activated IKK, and phosphorylated p65 in the axon initial segment of neurons. Mol. Cell. Neurosci 33, 68–80. [PubMed: 16875840]

Somogyi P (1977). A specific "axo-axonal" interneuron in the visual cortex of the rat. Brain Res. 136, 345–350. [PubMed: 922488]

Somogyi P, Katona L, Klausberger T, Lasztóczi B, and Viney TJ (2014). Temporal redistribution of inhibition over neuronal subcellular domains underlies state-dependent rhythmic change of excitability in the hippocampus. Philos. Trans. R. Soc. B Biol. Sci 369, 20120518.

Stark E, Eichler R, Roux L, Fujisawa S, Rotstein HG, and Buzsáki G (2013). Inhibition-Induced Theta Resonance in Cortical Circuits. Neuron 80, 1263–1276. [PubMed: 24314731]

Stuart G, Schiller J, and Sakmann B (1997). Action potential initiation and propagation in rat neocortical pyramidal neurons. J. Physiol 505, 617–632. [PubMed: 9457640]

Szabadics J, Varga C, Molnár G, Oláh S, Barzó P, and Tamás G (2006). Excitatory effect of GABAergic axo-axonic cells in cortical microcircuits. Science 311, 233–235. [PubMed: 16410524]

Szabo GG, Du X, Oijala M, Varga C, Parent JM, and Soltesz I (2017). Extended Interneuronal Network of the Dentate Gyrus. Cell Rep. 20, 1262–1268. [PubMed: 28793251]

Szentagothai J, and Arbib MA (1974). Conceptual models of neural organization. Neurosci. Res. Program Bull 12, 510.

Taniguchi H, He M, Wu P, Kim S, Paik R, Sugino K, Kvitsani D, Fu Y, Lu J, Lin Y, et al. (2011). A Resource of Cre Driver Lines for Genetic Targeting of GABAergic Neurons in Cerebral Cortex. Neuron 71, 995–1013. [PubMed: 21943598]

Taniguchi H, Lu J, and Huang ZJ (2013). The spatial and temporal origin of chandelier cells in mouse neocortex. Science 339, 70–74. [PubMed: 23180771]

Ting JT, Daigle TL, Chen Q, and Feng G (2014). Acute brain slice methods for adult and aging animals: application of targeted patch clamp analysis and optogenetics. Methods Mol. Biol 1183, 221–242. [PubMed: 25023312]

Vanderwolf CH (1969). Hippocampal electrical activity and voluntary movement in the rat. Electroencephalogr. Clin. Neurophysiol 26, 407–418. [PubMed: 4183562]

Varga C, Oijala M, Lish J, Szabo GG, Bezaire M, Marchionni I, Golshani P, and Soltesz I (2014). Functional fission of parvalbumin interneuron classes during fast network events. Elife 3, 1–23.

Viney TJ, Lasztoczi B, Katona L, Crump MG, Tukker JJ, Klausberger T, and Somogyi P (2013). Network state-dependent inhibition of identified hippocampal CA3 axo-axonic cells in vivo. Nat. Neurosci 16, 1802–1811. [PubMed: 24141313]

Wang X-J, and Buzsáki G (1996). Gamma Oscillation by Synaptic Inhibition in a Hippocampal Interneuronal Network Model. J. Neurosci 16, 6402–6413. [PubMed: 8815919]

Wang X, Tucciarone J, Jiang S, Yin F, Wang BS, Wang D, Jia Y, Jia X, Li Y, Yang T, et al. (2019). Genetic Single Neuron Anatomy Reveals Fine Granularity of Cortical Axo-Axonic Cells. Cell Rep. 26, 3145–3159.e5. [PubMed: 30865900]

Whishaw IQ, and Vanderwolf CH (1971). Hippocampal EEG and behavior: effects of variation in body temperature and relation of EEG to vibrissae movement, swimming and shivering. Physiol. Behav 6, 391–397. [PubMed: 5148749]

Woodruff A, Xu Q, Anderson SA, and Yuste R (2009). Depolarizing effect of neocortical chandelier neurons. Front. Neural Circuits 3, 15. [PubMed: 19876404]

Woodruff AR, McGarry LM, Vogels TP, Inan M, Anderson SA, and Yuste R (2011). State-dependent function of neocortical chandelier cells. J. Neurosci 31, 17872–17886. [PubMed: 22159102]

Yang L, Lee K, Villagracia J, and Masmanidis SC (2020). Open source silicon microprobes for high throughput neural recording. J. Neural Eng 17, 016036. [PubMed: 31731284]

Zhu Y, Stornetta RL, and Zhu JJ (2004). Chandelier cells control excessive cortical excitation: Characteristics of whisker-evoked synaptic responses of layer 2/3 nonpyramidal and pyramidal neurons. J. Neurosci 24, 5101–5108. [PubMed: 15175379]

Author Manuscript Author Manuscript Author Manuscript Author Manuscript

Highlights

- CA1 axo-axonic cells (AACs) are selectively labeled in Unc5b-2A-CreERT2 mice
- AACs are activated by locomotion or whisking in awake mice
- AACs exert inhibitory postsynaptic effects on CA1 pyramidal cells in vivo
- AAC optogenetic silencing induces novel place fields in pyramidal cells

Author Manuscript Author Manuscript Author Manuscript Author Manuscript

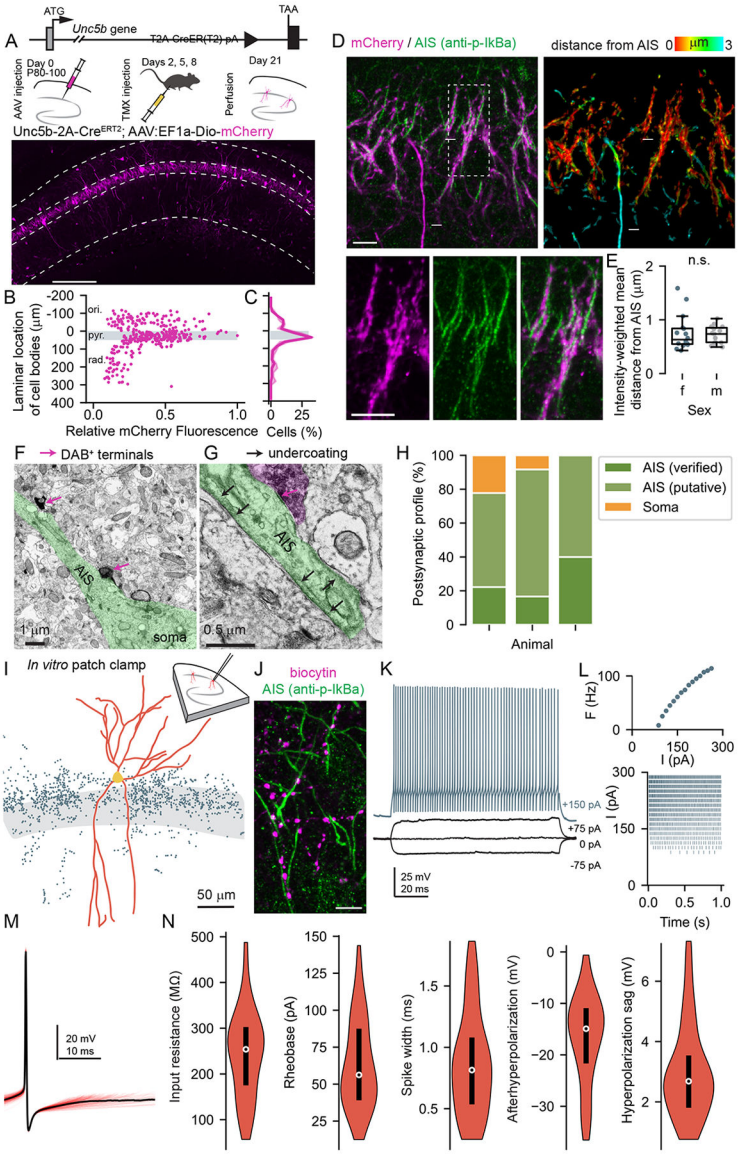

Figure 1. Unc5b allows selective genetic targeting of AACs in the adult mouse hippocampal area CA1

A) Schematic of the generation of the Unc5b-2A-CreERT2 knock-in driver mouse, and the labeling strategy in adult mice. Confocal micrograph shows expression after viral conditional labeling in the CA1.

B) Fluorescence intensity and laminar position of somata (markers: individual cells, n = 351)

C) Histogram of laminar soma distribution (median ± IQR, n = 6 mice).

D) Maximum intensity projection of a confocal micrograph shows immunostaining of the mCherry-labeled processes and the axon initial segment (AIS) marker phospho-IkBα (top left). The boxed region is shown enlarged (bottom). The distance of each mCherry-positive voxel from the nearest p-IkBα-positive voxel is indicated by hue (top right, see color scale, see also Fig. S1). Note that axons (ax) were proximal to AISs (red), whereas a putative dendrite (d), which is not expected to target AISs, was not (blue).

Author Manuscript Author Manuscript Author Manuscript Author Manuscript

E) Intensity-weighted average distance of positive voxels from AIS was similar between male and female mice (Mann-Whitney U test, U = 107, p = 0.31, n = 31 images from 4 male and 4 female mice).

F) Electron micrograph of immunostained boutons of Unc5b-AACs (arrows) impinging on an AIS.

G) Electron micrograph shows an immunopositive bouton (magenta) making a symmetric synapse with an AIS (green), identified by the presence of an electron dense undercoating (black arrows).

H) Percentage of immunopositive boutons targeting particular postsynaptic elements (n = 27 synapses, 3 animals).

I) Fluorescence-targeted patch-clamp recording of Unc5b-AACs. Example of a reconstruction (dendrites: red, axonal varicosities: grey, str. pyramidale: light grey).

J) Biocytin-filled boutons of the neuron shown in *G* targeted AISs.

K) Representative responses of an Unc5b-AAC during current steps (1 s-long hyperpolarizing and depolarizing square pulses, the +150 pA trace is separated for visibility). Note this is a different cell from panels *G-H*.

L) The F-I curve shows action potential frequencies during 1 s depolarizing current steps of the cell in *I*, individual action potential times are shown on a raster plot.

M) Aligned action potential waveform of the cell in *I-J* (red: individual events, black: average).

N) Distribution of intrinsic property features. Violin plots show kernel density; white markers: median; black bars: IQR. n = 50 AACs from 9 mice.

Author Manuscript Author Manuscript Author Manuscript Author Manuscript

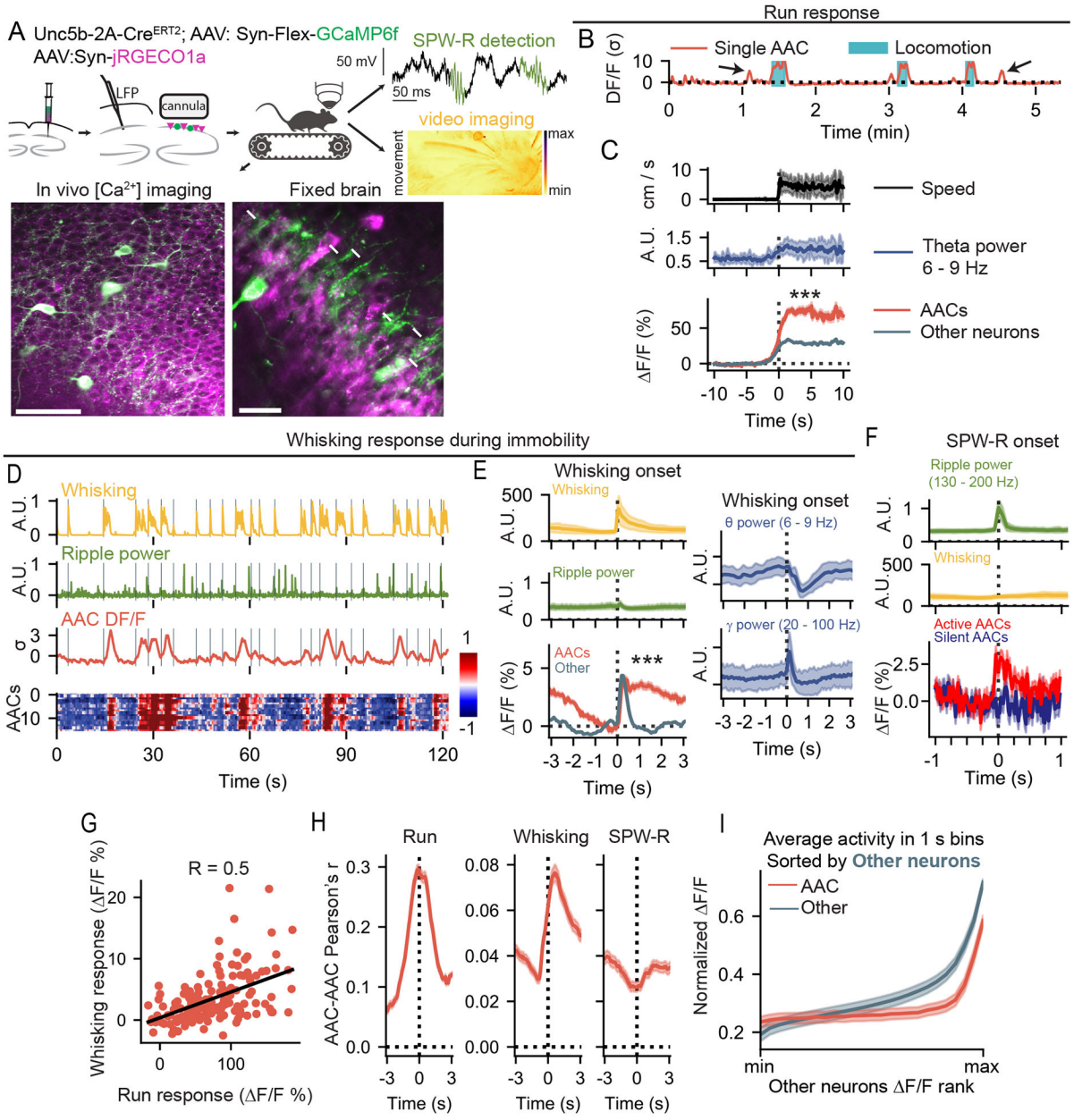

Figure 2. Brain state-specific AAC recruitment in vivo

A) Experimental strategy for *in vivo* two-photon calcium imaging from Unc5b-AACs, combined with correlated CA1 LFP and video recording. Green sections of LFP trace show examples of automatically detected SPW-R events. The average movement map of whisking events is shown (see also Fig. S2). White arrows depict AAC axonal cartridges visualized post hoc.

B) Fluorescence trace from a representative AAC shows activation of the cell during locomotion, as well as transient activity during immobility (arrows). Temporal smoothing (1 s exponentially weighted moving average) is applied to the traces on *B* and *D*.

C) AAC response to locomotion onset was greater than average neuronal response (see also Fig. S2). Speed: mean ± SD; ΔF/F: mean ± SEM.

Author Manuscript Author Manuscript Author Manuscript Author Manuscript

D) Fluorescence from a single representative AAC shows activation of the cell during immobility, which coincided with whisking episodes, but not with SPW-Rs. The heatmap shows the synchronous activation of all AACs within the field of view. Gray vertical lines show whisking event onset. Ripple-band power (130-200 Hz envelope integrated per imaging frame) and whisking activity (sum of movement map in whisker pad) are normalized.

E) AAC response to whisking events was greater than average neuronal response (see also Fig. S2). The baseline (−1 to 0 s) is subtracted from the ΔF/F traces on *E* and *F*. The apparent drop in AAC activity before events may reflect clustering of the events. Changes in LFP power are shown during the same events, mean ± SD.

F) AAC response to SPW-R events is shown with subframe precision (20ms binning, mean ± SEM). AACs were classified based on the rate of detected activity in SPW-Rs (silent: <= 5%, active: >5%). Average “silent” AAC activity during all SPW-R events is shown in blue, average “active” AAC activations shown in red. Whisking was low during SPW-Rs (ripple power and whisking shown as mean ± SD). See also Fig. S2.

G) Correlated run- and whisking responses of individual AACs (Spearman’s $R = 0.50$, $p < 0.001$, $n = 159$ AACs).

H) Average of pairwise AAC-AAC correlations in rolling symmetric windows (± 1 s) is transiently increased at run- and whisking-, but not SPW-R onset (mean ± SEM).

I) Scaling of AAC activity with network activity (see also Fig. S2). Normalized activity of each cell type in 1 s episodes after averaging the traces into equally sized bins according to rank by ΔF/F of non-AAC neurons (n = 36 sessions, 7 animals).

Author Manuscript Author Manuscript Author Manuscript Author Manuscript

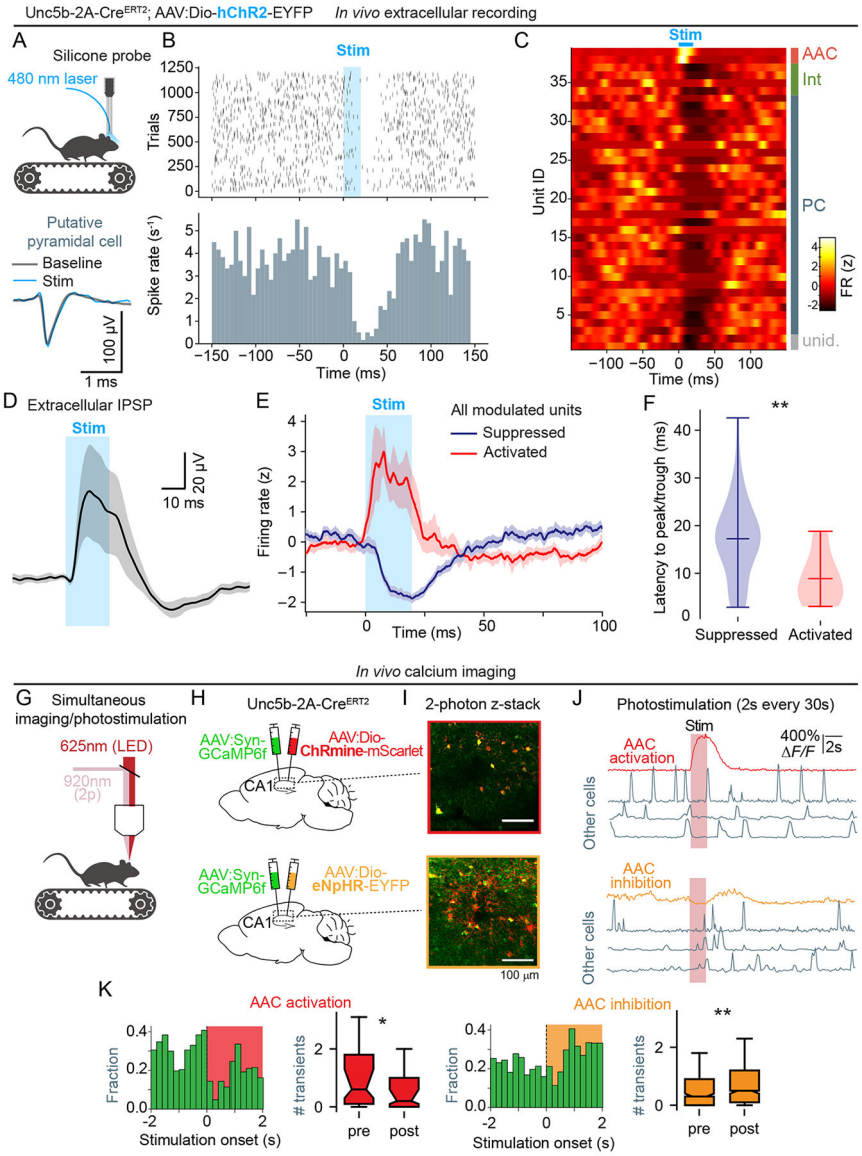

Figure 3. AACs inhibit CA1 pyramidal cell activity in vivo

A) Schematic of the experiment design for *in vivo* silicone probe extracellular recording. Excitatory opsin (hChR2) was expressed in Unc5b-AACs. Spike waveforms of an example unit (putative PC) are shown. Identical spike waveforms during and outside stimulus episodes indicate negligible light artefact.

B) Top: spike raster plot from the same unit across all trials (20 ms light pulses at 2 Hz), aligned on stimulus onset. Bottom: peri-stimulus time histogram shows suppression of spiking by the light pulse.

C) Firing rates of all units identified by spike sorting from a single recording session. Units driven by the stimulus (Zeta method, $p < 0.01$) were identified as AACs (see also Fig. S3 and Methods). Note that non-opto-tagged units classified as either interneurons (Int) or PCs were similarly suppressed by the stimulus. Representative of 17 experiments from 8 mice, 690 cells in total, 12 AACs.

Author Manuscript Author Manuscript Author Manuscript Author Manuscript

D) Stimulus-triggered average of LFP traces recorded in the stratum pyramidale (n = 17 experiments from 8 mice) showing photostimulation-evoked extracellular potentials (mean ± SD).

E) Average firing rate change in significantly modulated units (mean ± 95% CI, Zeta $p < 0.01$, latency to peak/trough between 1 and 50 ms. Out of 705 PCs (from 8 mice), 14.9 ± 9.8% showed significantly suppressed firing rates response to AAC activation, while 2.4 ± 2.1% displayed elevated firing rates.

F) Latency to trough in suppressed units (n = 56) was longer compared to latency to peak in activated units (n = 12, $p < 0.001$, permutation test). Violins show kernel density, whiskers show mean and range.

G) Schematic of the experimental design for *in vivo* two-photon calcium imaging and acute time-locked optogenetic manipulation of AACs in head-fixed mice running on a linear treadmill.

H) GCaMP6f was expressed in all neurons, while excitatory (ChRmine, top) or inhibitory (eNpHR, bottom) opsin was expressed in Unc5b-AACs.

I) Maximum intensity projections of example CA1 fields-of-view from eNpHR- or ChRmine-injected animals.

J) Effect of activation (top) or inhibition (bottom) on an example AAC (colored traces) and example non-AAC (putative pyramidal) neurons (grey traces) upon photostimulation.

K) Peri-stimulus time histogram of population activity showing an inhibitory effect of 2 s AAC activation (left) and a disinhibitory effect of AAC silencing (right) on calcium transient rates (>150% ΔF/F). Stimulation significantly altered transient rates in units with > 1 transient during the pre or post period (likelihood ratio test, $X^2(1) = 5.7$, $p = 0.017$, n = 57 units, 4 mice (ChRmine); $X^2(1) = 4.5$, $p = 0.035$, n = 493 units, 4 mice (eNpHR)). Asterisks indicate significant difference in Wilcoxon signed rank test on paired samples (ChRmine: $V = 484$, $p = 0.01$; eNpHR: $V = 59178$, $p = 0.009$).

Author Manuscript Author Manuscript Author Manuscript Author Manuscript

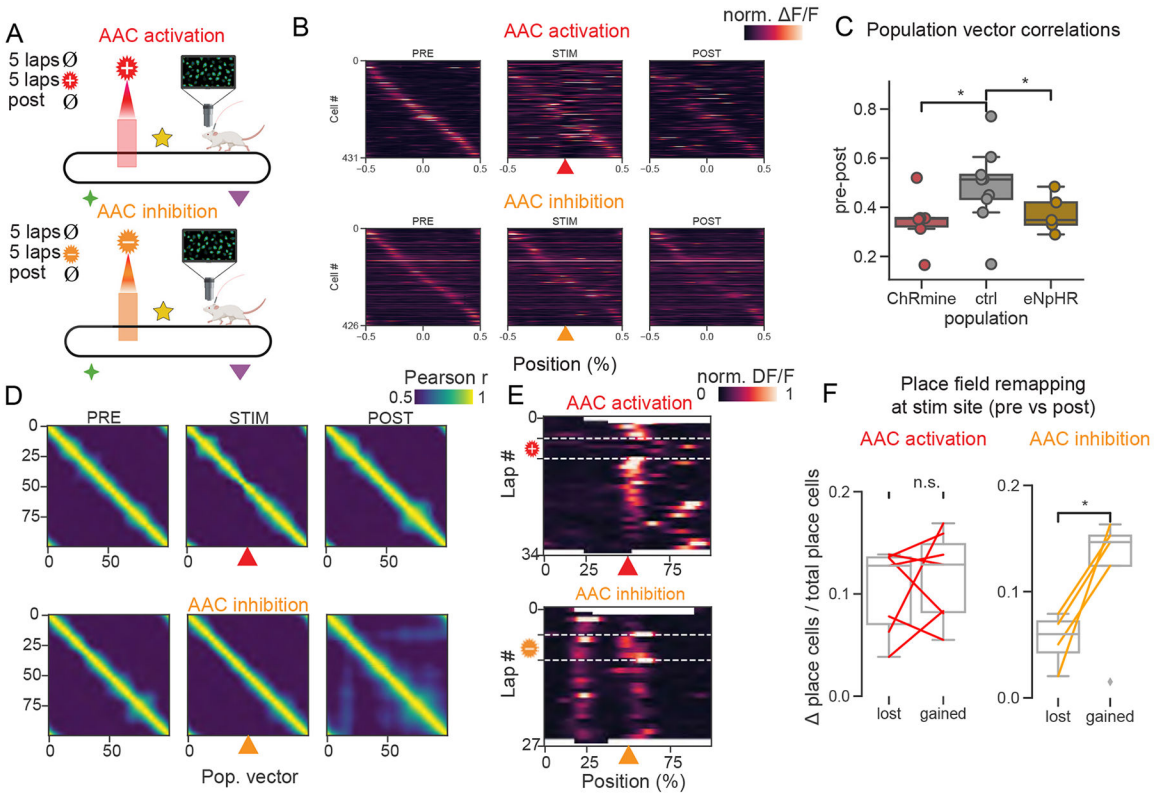

Figure 4. AAC optogenetic manipulation induces place field remapping

A) Simultaneous two-photon calcium imaging and acute, spatially locked optogenetic manipulation of Unc5b-AACs in head-fixed mice running on a cue-rich linear treadmill. In a 15-minute recording session, mice ran 5-10 laps with no manipulation (PRE), then photostimulation was applied in a fixed spatial location on the treadmill for 5 laps (STIM), finally the animal ran with no manipulation for the remainder of the session (POST).

B) Spatial tuning curves of place cells during PRE, STIM, and POST phases in sessions with either AAC activation (top) or inhibition (bottom), sorted by place field peak in PRE, normalized per cell. Laps are centered on stimulus location on all panels.

C) The treadmill was segmented into 100 spatial bins (2 cm wide) and population vectors were calculated for each bin. Change in mean population vector correlations in response to AAC excitation or inhibition (PRE-POST) were compared to sessions with the same temporal structure (5 PRE, 5 STIM, POST) but without light stimulation. Both AAC excitation and inhibition cause significant population-level decorrelation and remapping among place cells (ChRmine vs Ctrl: p=0.026, unpaired t-test; eNpHR vs Ctrl: p=0.04, unpaired t-test; N=6 mice in ChRmine, 9 in Ctrl, 5 in eNpHR). Box-and-whisker plots: 25th percentile, median, 75th percentile, and range (excluding outliers) of individual mouse-averaged tuning curve correlations (dots).

D) AAC activation suppressed place fields in the photostimulation zone (white arrow, top), which did not persist into the POST phase. In contrast, AAC silencing induced new place field formation in the photostimulation zone (white arrow, bottom), which persisted into the POST phase.

Author Manuscript Author Manuscript Author Manuscript Author Manuscript

E) Example place cells showing suppression of in-field activity during AAC activation (white arrow, top) and novel place field induction during AAC inhibition (white arrow, bottom). White areas represent missing data due to incomplete first and last laps.
F) AAC stimulation produces no net change in the number of photostimulation zone place fields from PRE to POST (paired t-test, p=0.50, n = 7 mice, see also Fig. S4). In contrast, AAC silencing generated additional place fields (paired t-test, p=0.012, n = 4 mice). Note, most cells do not have a place field in the photostimulation zone.

Author Manuscript Author Manuscript Author Manuscript Author Manuscript

KEY RESOURCES TABLE

REAGENT or RESOURCE	SOURCE	IDENTIFIER
Antibodies		
Chicken anti-mCherry	EnCor Biotechnology	Cat# CPCA-mCherry, RRID: AB_2572308
Rabbit anti-phospho-IκBα	Cell Signaling Technology	Cat# 2859, RRID: AB_561111
Chicken anti-GFP	Aves	Cat# GFP-1020, RRID: AB_10000240
Guinea pig anti-parvalbumin	Swant	Cat# GP72, RRID: AB_2665495
Chicken anti-parvalbumin	gift from Susan Brenner-Morton	N/A
Rabbit anti-SATB1	Abcam	Cat# ab70004, RRID: AB_1270545
Bacterial and virus strains		
AAV1.Syn.Flex.GCaMP6f.WPRE.SV40	UPenn Viral Vector Core	N/A
AAV5-EF1a-DIO-mCherry	UNC Core	N/A
AAV5-EF1a-DIO-hChR2(H134R)-mCherry-WPRE-pA	UNC Core	N/A
AAV1.Syn.NES-jRGECO1a.WPRE.SV40	UPenn Viral Vector Core	N/A
AAV1.Syn.Flex.NES-jRGECO1a.WPRE.SV40	UPenn Viral Vector Core	N/A
AAV9-CAG-DIO-ChroME-ST-P2A-H2B-mRuby3	Mardinly et al Nat Neurosci. 2018 Jun;21(6):881-893.	Addgene AAV9 particles produced from pAAV-CAG-DIO-ChroME-ST-P2A-H2B-mRuby3 (#108912)
AAV1-Ef1a-DIO-eNpHR3.0-EYFP	Gradinaru et al Cell. 2010 Apr 2. 141(1):154-65.	Addgene AAV1 particles produced from pAAV-Ef1a-DIO eNpHR 3.0-EYFP (#26966)
AAV1-Ef1a-DIO-ChRmine-mScarlet	gift from K. Deisseroth	N/A
AAVDJ-CaMKIIa-GCaMP6f	UNC Core	N/A
Biological samples		
Chemicals, peptides, and recombinant proteins		
Tamoxifen	Sigma	Cat# 06734
Critical commercial assays		
Deposited data		
Source data for figures	This study; Mendeley Data	DOI: 10.17632/nsn63ybw9d.1
Experimental models: Cell lines		

Author Manuscript Author Manuscript Author Manuscript Author Manuscript

REAGENT or RESOURCE	SOURCE	IDENTIFIER
Experimental models: Organisms/strains		
Unc5b-CreER	This study	N/A
Oligonucleotides		
Recombinant DNA		
Software and algorithms		
Custom scripts	This study; Zenodo	DOI: 10.5281/zenodo.5504358
MountainSort	Chung et al., 2017; https://doi.org/10.1016/j.neuron.2017.08.030	https://github.com/flatironinstitute/mountainsort.git
Kilosort2	Steinmetz et al., 2021; DOI: 10.1126/science.abf4588	https://github.com/MouseLand/Kilosort
Phy	Cyrille Rossant	https://github.com/cortex-lab/phy
Matlab	Mathworks	Version: R2019b
ZEN	Zeiss	Version: 2012 SP5 FP1 v14
Scanbox	Neurolabware	Version: v4.6
ImageJ/FIJI	NIH	Version: v1.52p
Python	Python.org	Version: v3.6
RStudio	RStudio	Version: 1.4.1106
sima (Python)	Kaifosh et al., 2014; PMID: 25295002	https://github.com/losonczylab/sima.git
OASIS (Python)	Friedrich, Zhou and Paninski, 2017, PMID: 28291787	https://github.com/j-friedrich/OASIS.git
Suite2p (Python)	Pachitariu et al., 2017; https://doi.org/10.1101/061507	https://www.suite2p.org/
TreFiDe	Buchanan et al., 2019; https://doi.org/10.1101/334706	https://github.com/ikinsella/trefide.git
pClamp	Molecular Devices	Version: v10.7.0.3
Clampfit	Molecular Devices	Version: v10.7.0.3
Other		